

Diff-Ensembler: Learning to Ensemble 2D Diffusion Models for Volume-to-Volume Medical Image Translation

Xiyue Zhu¹ Dou Hoon Kwark¹ Ruike Zhu¹ Kaiwen Hong¹ Yiqi Tao¹
 Shirui Luo² Yudu Li¹ Zhi-Pei Liang¹ Volodymyr Kindratenko^{1,2}
¹University of Illinois at Urbana-Champaign ²National Center for Supercomputing Applications

Abstract

Despite success in volume-to-volume translations in medical images, most existing models struggle to effectively capture the inherent volumetric distribution using 3D representations. The current state-of-the-art approach combines multiple 2D-based networks through weighted averaging, thereby neglecting the 3D spatial structures. Directly training 3D models in medical imaging presents significant challenges due to high computational demands and the need for large-scale datasets. To address these challenges, we introduce *Diff-Ensembler*, a novel hybrid 2D-3D model for efficient and effective volumetric translations by ensembling perpendicularly trained 2D diffusion models with a 3D network in each diffusion step. Moreover, our model can naturally be used to ensemble diffusion models conditioned on different modalities, allowing flexible and accurate fusion of input conditions. Extensive experiments demonstrate that *Diff-Ensembler* attains superior accuracy and volumetric realism in 3D medical image super-resolution and modality translation. We further demonstrate the strength of our model’s volumetric realism using tumor segmentation as a downstream task.

1. Introduction

Volume-to-volume image translation is highly useful for volumetric medical imaging, such as magnetic resonance imaging (MRI) and X-ray computed tomography (CT). It solves inverse problems of image reconstruction [15, 31, 49], handling sparse [24, 36], limited [8, 35], and/or noisy [8, 52] imaging data. It also supports image synthesis, where volume translation can convert images from one imaging modality to another, such as multi-contrast MRI [9, 42, 51, 53], CT-ultrasound [48], and MR-histopathology [28]. These models enable numerous downstream image processing tasks, ranging from image reconstruction [37] to analysis [1, 12]). Moreover, as suggested in previous work [11],

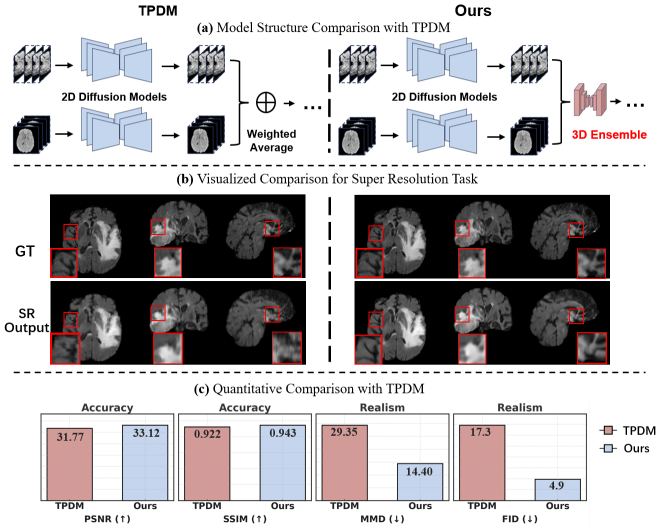


Figure 1. Comparison between TPDM (left) and Diff-Ensembler (right). Diff-Ensembler learns to ensemble pre-trained diffusion models with a 3D model, effectively utilizing 3D representations to model the 3D distribution. Our model thus shows better visual quality with 3D consistency and quantitatively demonstrates superior accuracy and realism metrics.

generating 3D realistic volume in such tasks is important since most models in downstream analysis tasks, such as tumor segmentation [16], are trained on 3D volumes.

Recent advances in volume-to-volume translation have introduced methods that combine perpendicular 2D diffusion models [4, 27], achieving improved accuracy and volumetric consistency. However, these methods cannot model the distribution of the entire volume since the generated images are produced by an averaging of the 2D networks without 3D representations, resulting in limited realism in 3D. Although 3D networks are more adept at capturing volumetric structures, previous works [11, 27] highlight substantial challenges in their increased demands for computational resources and large datasets that are costly to acquire in medical imaging. To the best of our knowledge, within the domain of 3D medical image inverse problems, no fully 3D models have

demonstrated superior accuracy over 2D-based models due to these practical limitations. Designing a 3D network of similar size with 2D models is suggested by [34], which is a promising approach given the rich 3D context and strong pre-trained 2D models. However, this is generally infeasible with existing 2D diffusion models[41], which require around 300 GB of GPU memory for training with extremely long training time. As a result, current 3D diffusion models [11] are designed to be much smaller with insufficient capacity to demonstrate competitive performance in inverse problems.

To effectively introduce 3D representations into volumetric translation, we present Diff-Ensembler, a pioneering model for volumetric translation that directly and effectively captures the distribution of 3D volumes. Diff-Ensembler adopts a two-stage training strategy: (1) It first trains multiple 2D diffusion models [40] on perpendicular planes. (2) It then utilizes a 3D fusion network to produce the final translation in each diffusion step. Meanwhile, using the alignment layers, the 3D ensemble network effectively uses the hierarchical feature maps from the 2D model. This mixture-of-experts (MoE) approach capitalizes on the strengths of both 2D and 3D networks, achieving highly accurate and spatially realistic 3D outputs. Moreover, Diff-Ensembler is able to decrease the capacity requirement for an accurate 3D diffusion model by introducing pre-trained 2D diffusion models in multiple slice directions, addressing the computational challenge of 3D diffusion models. Additionally, by ensembling diffusion models conditioned on various input modalities, Diff-Ensembler seamlessly supports multi-modality fusion.

The mathematical intuition of Diff-ensemblar lies in the properties of diffusion models and their associated score functions[44]. As the score function models the gradient of the probability distribution, it is inherently suitable for an iterative ensemble. Previous works [4, 6] also have demonstrated this by showing strong performance with a straightforward weighted averaging of score functions. Consequently, Diff-Ensembler replaces the weighted averaging process with a 3D network, enhancing robustness while addressing the computational demands of 3D models. To the best of our knowledge, Diff-ensemblar is the first work that uses a mixture-of-experts(MoE) model in the score function space, which provides new insights for diffusion models ensembling. Diff-ensemblar can also function as a plug-and-play mechanism compatible with various combinations of 2D models from previous studies [4, 6, 30], consistently delivering performance improvements across various 2D backbones.

The efficiency and effectiveness of Diff-ensemblar have been evaluated in various MRI image processing tasks on the BraTS [2] and HCP [10] dataset, including image super-resolution and modality translation. Our experimental results demonstrate that Diff-Ensembler performs superior volume translation over current state-of-the-art (SoTA) models. By

learning to ensemble perpendicular 2D models conditioned on different input modalities, Diff-Ensembler shows strong performance without retraining new 2D models.

2. Related Work

3D medical image generation and translation. Attempts have been made to generate dense 3D volumes for medical imaging. Direct 3D-based diffusion models [11, 34] face difficulties due to high computational and dataset demands, limiting them to smaller models that result in moderate accuracy in tasks like super-resolution. Patch-wise, slice-wise, or cascaded generation strategies have been utilized to accommodate high-dimensional data within the constraints of limited GPU memory [47]. This cascade approach introduces several drawbacks. The multi-stage nature of the process can lead to compounded errors, where initial inaccuracies in the low-resolution base are propagated and amplified during the refinement stages. Additionally, the patch-based refinement often struggles with maintaining global consistency across the image, resulting in visible seams or inconsistencies in the final output. **Latent 3D models** [11, 25, 56] have been exploited to reduce the degrees of freedom of 3D volume representation by compressing the entire 3D data into a low-dimensional latent space. Subsequently, a generative model is constructed within this compressed latent space. Also, the process of reducing dimensionality can lead to substantial reconstruction errors, compromising the accuracy and fidelity of the generated images. **Sequential slice generation from Auto-regressive models** [38, 57] or **simultaneous multiple-slice generation** may mitigate this issue of error accumulation over slices. Yet, these approaches face difficulties in sustaining coherence for long-range structures. More related to our approach, **integrating multiple 2D models trained along perpendicular directions** is a promising approach. TPDM [27] first proposes to combine two perpendicular 2D diffusion models to improve 3D imaging, where the weighted average of scores from pre-trained 2D models estimates the score function of a 3D model. Building on this concept, following up works, such as TOSM [30] and MADM [4], further improve the model performance by including 2D models in all three directions and using multiple consecutive 2D slices in 2D models. These models generate highly accurate results by effectively leveraging the high-resolution information in each 2D plane. Directly inspired by these works, we use a 3D model to ensemble multiple perpendicularly trained 2D models instead of the weighted average. This results in a more accurate and realistic 3D generation since the 3D ensembler network can introduce 3D features and directly model the 3D distribution.

Model ensembling. Ensemble techniques, which include key methodologies such as bagging, boosting, and stacking, have been developed further through specialized algorithms like Random Forest, AdaBoost, XGBoost, and Mixture of

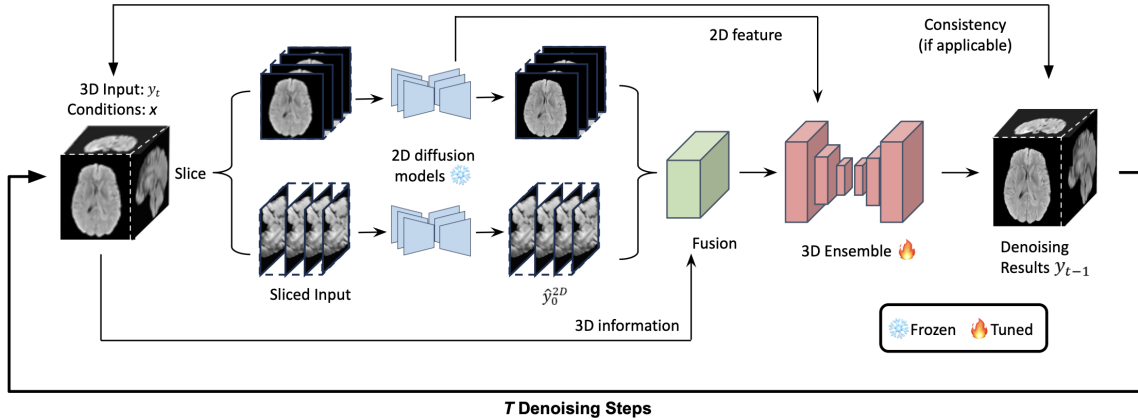


Figure 2. Overview of the Diff-Ensembler inference process for volume-to-volume translation. At each denoising step, the process begins with two pre-trained high-capacity 2D models that provide initial estimations. Subsequently, a 3D network integrates these estimations, learning to effectively ensemble the 2D outputs while incorporating 3D features to model spatial distributions. By integrating the initial input, the estimated results from the 2D models, and their feature maps as additional evidence, empirically, the required capacity of the 3D model is significantly reduced, enabling more efficient capture of the 3D distribution.

Experts (MoE). These techniques have not only excelled in general domains but have also demonstrated remarkable efficacy in medical image analysis, particularly in areas such as brain tumor segmentation [16, 55], hypertension detection [13], and kidney stone identification [23]. More recent research underscores the potential of ensembles as an effective strategy for scaling up large models, further broadening the scope and application of ensemble methods in advanced computational tasks [21].

Diffusion model ensembling. Recently, diffusion models have shown great success. The ensembling methods for diffusion models have become a useful research topic. Most current works use weighted averages to ensemble different branches of diffusion models [5, 27]. Collaborative Diffusion [19] is a learning-based ensembling method for diffusion; it trains an auxiliary model to estimate the confidence score for each branch of diffusion and ensemble based on the score. In this work, our approach uses an MoE architecture that uses information across all branches of diffusion models. This under-explored approach provides new insights for advancing diffusion model ensembling.

3. Diffusion Ensembler in 3D

Problem formulation. We formulate the volume-to-volume translation task as conditional sampling, aiming to generate the target medical image volumes $\mathbf{y} \in \mathbb{R}^{b_1, b_2, b_3}$ from given volumes $\mathbf{x} \in \mathbb{R}^{c, b_1, b_2, b_3}$ where b_1, b_2 and b_3 denote the size along 3 spatial dimensions, and c is the number of given volumes. In addition, we aim to effectively model the 3D volumetric distribution directly with 3D representations. The input, \mathbf{x} , could contain a low-resolution volume and/or a volume of another modality.

3.1. Overall Framework of Diff-Ensembler

We designed the Diff-Ensembler as a conditional diffusion model. Following DDPM and Palette [18, 41], our model gradually adds Gaussian noise to the target image in the training dataset during the *forward* or *diffusion process* as follows:

$$q(\mathbf{y}_t | \mathbf{y}_{t-1}) = \mathcal{N}(\mathbf{y}_t; \sqrt{1 - \beta_t} \mathbf{y}_{t-1}, \beta_t \mathbf{I}), \quad (1)$$

$$q(\mathbf{y}_T | \mathbf{y}_0) = q(\mathbf{y}_0) \prod_{t=1}^T q(\mathbf{y}_t | \mathbf{y}_{t-1})$$

where $\mathbf{y}_0 \sim q(\mathbf{y})$ is the target image and β_t is the variance of noise added at timestep t . The forward process produces a sequence of increasingly noisy variables $\mathbf{y}_1, \dots, \mathbf{y}_T$, after sufficient noising steps, the process reaches a pure Gaussian noise, *i.e.*, $\mathbf{y}_T \sim \mathcal{N}(\mathbf{0}, \mathbf{I})$.

During **training**, our denoising diffusion model, $\epsilon_\theta(\mathbf{y}_t, \mathbf{x}, t)$, is trained to predict the noise added into \mathbf{y} , given \mathbf{y}_t . Demonstrated effectively in works [40], the sampling process can be guided by concatenating the noisy image \mathbf{y}_t with condition \mathbf{x} . The conditioning denoising process is then to optimize $\epsilon_\theta(\mathbf{y}_t, \mathbf{x}, t)$ by:

$$\mathcal{L}_t = \left\| \underbrace{\epsilon_\theta(\sqrt{\alpha_t} \mathbf{y}_0 + \sqrt{1 - \alpha_t} \epsilon, \mathbf{x}, t)}_{\mathbf{y}_t} - \epsilon \right\|_2^2 \quad (2)$$

where $\alpha_t := \prod_{i=1}^t (1 - \beta_i)$, and we sample $\mathbf{y}_0, \mathbf{x} \sim p(\mathbf{y}_0, \mathbf{x}), \epsilon \sim \mathcal{N}(\mathbf{0}, \mathbf{I})$.

During **sampling** in the *reverse* or *generative process*, we also follow Palette [41] to generate images by iteratively removing the added noise in the sequence $\mathbf{y}_{T-1}, \dots, \mathbf{y}_1, \mathbf{y}_0$, from a standard Gaussian prior $\mathbf{y}_T \sim \mathcal{N}(\mathbf{0}, \mathbf{I})$. In addition, inspired by [7, 43, 45], we explore self-consistency for solving inverse problems. More specifically, in each diffusion sampling step, we estimate noise with our denoising

model $\epsilon_\theta(\mathbf{y}_t, \mathbf{x}, t)$. Therefore, we have the estimated $\hat{\mathbf{y}}_0(t)$ at t -th denoising step as $\hat{\mathbf{y}}_0(t) := \frac{\mathbf{y}_t - \sqrt{1 - \alpha_t} \epsilon_\theta(\mathbf{y}_t, \mathbf{x}, t)}{\sqrt{\alpha_t}}$. In inverse problems, conditional input \mathbf{x} is obtained through a known linear degradation process $\mathbf{x} = A\mathbf{y}$. At each diffusion step, we project the estimated $\hat{\mathbf{y}}_0(t)$ to a plausible $\hat{\mathbf{y}}_0(t)$, such that $\mathbf{x} = A\hat{\mathbf{y}}_0$. To perform this projection, we have $\hat{\mathbf{y}}_0(t) \leftarrow \hat{\mathbf{y}}_0(t) - A^T(AA^T)^{-1}(A\hat{\mathbf{y}}_0(t) - \mathbf{x})$. After the consistency projection, we obtain \mathbf{y}_{t-1} by adding noise back: $\mathbf{y}_{t-1} = \sqrt{\alpha_{t-1}}\hat{\mathbf{y}}_0(t) + \sqrt{1 - \alpha_{t-1}}\epsilon$. We include more mathematic details of the projection in Sec. 13.

The key component of this work lies in our denoising network $\epsilon_\theta(\mathbf{y}_t, \mathbf{x}, t)$, which presents a novel integration of perpendicular 2D diffusion models and a 3D ensemble model. In particular, our model ϵ_θ consists of two 2D diffusion denoising models, $\epsilon_{\theta_a}^{2D(a)}$ and $\epsilon_{\theta_b}^{2D(b)}$, and a 3D diffusion denoising model, $\epsilon_{\theta_{3D}}^{3D}$, with θ_a , θ_b , and θ_{3D} being their trainable parameters, respectively. The 3D network is conditioned on two 2D diffusion models to alleviate computational challenges. The 2D models are trained to capture 2D image distributions along orthogonal planes, providing complementary views of the volumetric data. This design effectively constrains the 3D model, reducing the risk of overfitting and promoting faster convergence. We refer to this hybrid 2D/3D volumetric generative model as Diff-Ensembler. Fig. 2 provides a schematic overview of Diff-Ensembler. The modeling and implementation are provided in the following.

3.2. 2D Diffusion Models

The two 2D diffusion models, $\epsilon_{\theta_a}^{2D(a)}$ and $\epsilon_{\theta_b}^{2D(b)}$, are trained on two perpendicular slices of the volumes using a standard conditional diffusion framework [40]. We take gradient descent steps on the following objectives for both 2D diffusion models during training:

$$\begin{aligned} \nabla_{\theta_a} \|\epsilon_{\theta_a}^{2D(a)}(\mathbf{y}_t[:, i, :], \mathbf{x}[:, i, :], t) - \epsilon\|_2^2 \\ \nabla_{\theta_b} \|\epsilon_{\theta_b}^{2D(b)}(\mathbf{y}_t[:, :, j], \mathbf{x}[:, :, j], t) - \epsilon\|_2^2 \end{aligned} \quad (3)$$

Here, i and j are the indices for the slices along two perpendicular planes, which are sampled uniformly: $i \sim \text{Uniform}\{0, \dots, b_2\}$, $j \sim \text{Uniform}\{0, \dots, b_3\}$. After proper training, the high-capacity 2D model can provide a decently accurate estimation of ϵ for every volume slice.

3.3. 3D Ensembling Model

The 3D ensembling model, $\epsilon_{\theta_{3D}}^{3D}$, is trained to fuse the pre-trained 2D diffusion models to capture the desired volumetric image distributions. In this stage, we first obtain the inference results, $\hat{\mathbf{Y}}^{2D(a)}$ and $\hat{\mathbf{Y}}^{2D(b)}$, from the 2D diffusion models, $\epsilon_{\theta_a}^{2D(a)}$ and $\epsilon_{\theta_b}^{2D(b)}$ by iterating through the sliced directions:

$$\begin{aligned} \hat{\mathbf{Y}}^{2D(a)}[:, i, :] &= \epsilon_{\theta_a}^{2D(a)}(\mathbf{y}_t[:, i, :], \mathbf{x}[:, i, :], t) \text{ for } i \in [0, b_2) \\ \hat{\mathbf{Y}}^{2D(b)}[:, :, j] &= \epsilon_{\theta_b}^{2D(b)}(\mathbf{y}_t[:, :, j], \mathbf{x}[:, :, j], t) \text{ for } j \in [0, b_3) \end{aligned} \quad (4)$$

During training of the 3D diffusion model, both 2D models return $\hat{\mathbf{Y}}$'s, which contains the predicted noise and a hierarchical feature map of the model: $\hat{\mathbf{Y}}^{2D(a)} = (\hat{\epsilon}^{2D(a)}, \mathcal{F}^{2D(a)})$, $\hat{\mathbf{Y}}^{2D(b)} = (\hat{\epsilon}^{2D(b)}, \mathcal{F}^{2D(b)})$.

The 3D model is designed to effectively ensemble the outputs of multiple 2D models through a Mixture-of-Experts framework. Specifically, at each diffusion step, the 3D model takes as input the original image \mathbf{x} , the noisy intermediate state \mathbf{y}_t , and the noise estimation $\hat{\epsilon}$ obtained from the 2D diffusion models. This approach leverages the complementary strengths of 2D and 3D networks, resulting in highly accurate and spatially consistent 3D reconstructions. Furthermore, feature maps \mathcal{F} from the 2D models are incorporated as supplementary information to enhance the ensembling process. (see Fig. 2). These feature maps capture rich, multi-scale representations from the 2D diffusion processes, serving as auxiliary evidence that mitigates the risk of information bottlenecks between the 2D and 3D stages. Such bottlenecks could otherwise limit the effectiveness of the ensemble and lead to sub-optimal performance. Thus, the 3D network is trained to perform the ensembling process using the following formulation using an L2 loss:

$$\nabla_{\theta_{3D}} \|\epsilon_{\theta_{3D}}^{3D}(\mathbf{y}_t, \mathbf{x}, \hat{\mathbf{Y}}^{2D(a)}, \hat{\mathbf{Y}}^{2D(b)}, t) - \epsilon\|_2^2 \quad (5)$$

As in Eq. 2, we sample $\mathbf{y}_0, \mathbf{x} \sim p(\mathbf{y}_0, \mathbf{x})$, and $\epsilon \sim \mathcal{N}(\mathbf{0}, \mathbf{I})$. Although, the inference results from 2D models, $\hat{\mathbf{Y}}^{2D(a)}$ and $\hat{\mathbf{Y}}^{2D(b)}$, already help the training of the 3D model, 3D ensemble model still needs to be trained from scratch. To improve training speed, we initially pre-train the model on 3D patches, $(\mathbf{y}_0, \mathbf{x}) = \text{crop}(\mathbf{y}_0, \mathbf{x})$, and then fine-tune it on the full volumes. Due to the translation invariance of our convolution-based networks, we empirically find that a naively pre-train on the patches results in a decently good network initialization, thereby effectively improving the training convergence. While existing works, such as [50], could potentially enhance this patch-wise diffusion training process, we leave such optimizations for future work.

In this work, the **network architecture** of the 3D model, $\epsilon_{\theta_{3D}}^{3D}$, is designed following the 3D palette [11]. Specifically, we adopt a Unet-like denoising model with time-step embeddings and concatenate the 3D input \mathbf{x} , the noisy target \mathbf{y}_t , and the noise estimated by the 2D models $\hat{\epsilon}^{2D(a)}, \hat{\epsilon}^{2D(b)}$ as the input of the 3D model. In the encoder, each down-sampling block is enriched with corresponding feature maps from the features of both 2D models, $\mathcal{F}^{2D(a)}$, and $\mathcal{F}^{2D(b)}$. Inspired by [33], we feed these two features into two 1-layer convolution networks separately. These convolution layers map the two feature maps into the correct shapes required in the 3D model, while also aligning the 2D feature maps with the 3D feature maps through projection. The aligned feature maps are then added to the features in the 3D model. Additionally, rather than directly outputting the predicted noise, our 3D U-Net-like model produces two components:

a weight vector w , used to ensemble the estimations from the 2D models, and a residual term R , which is directly estimated by the 3D model. These two outputs are combined to form the final prediction:

$$\epsilon_{\theta_{3D}}^{3D}(\dots) = (0.5 + w)\hat{\epsilon}^{2D(a)} + (0.5 - w)\hat{\epsilon}^{2D(b)} + \lambda R \quad (6)$$

where λ is a hyperparameter, whereas w and R are of the same size as the target noise $\epsilon \in \mathbb{R}^{b_1, b_2, b_3}$. This design enables the model to dynamically select the more reliable 2D estimation based on 3D context and allows the 3D model to contribute its own 3D-specific content R . Meanwhile, a tunable weight parameter, λ , controls the model’s reliance on the 3D output, R . In addition, inspired by ControlNet [54], a zero-initialized convolution layer at the end of the model ensures smooth initialization, allowing training to start with an average weighting strategy and thereby stabilizing the 3D model training. The pseudocode for training and inference with Diff-Ensembler is provided in Algorithm 1 and Algorithm 2.

3.4. Multi-modality Fusion

In volumetric translation for medical imaging, the conditions for translating a new image can be multifaceted. For instance, DDMM-Synth [29] suggested using both MRI and low-resolution CT scans to produce high-resolution CT images. Training a separate model for each possible combination of input conditions would result in exponential time complexity, making it generally impractical. Therefore, a model that can integrate pre-trained models across diverse conditions provides significant advantages. Diff-Ensembler addresses this challenge by naturally integrating multiple diffusion models, each conditioned on individual modalities, through a 3D network architecture that functions similarly to fusing two 2D models described in 3.3. This approach leverages the efficiency of patch-wise pre-training for accelerated 3D training. To further enhance the speed of multi-modality fusion, we employ a smaller variant of our model, adjusting the number of channels in each layer. In this training, we do not leverage the feature maps \mathcal{F} from the 2D models, further optimizing computational efficiency.

4. Experiments

4.1. Experimental Setup

Datasets. We conducted experiments using the BraTS 2021 training dataset [2], which includes 1,251 volumetric brain scans with tumors across 4 modalities: FLAIR, T1, T1ce, and T2. Since ground-truth annotations are not publicly available for the validation and test datasets, we randomly divided the training dataset into a 0.8:0.2 split for training and evaluation purposes, allowing its use for downstream tasks as well. Each scan was center-cropped to a dimension of 192x192x152 to remove the blank background.

Algorithm 1 Training of Diff-Ensembler

```

1: repeat
2:    $(\mathbf{x}, \mathbf{y}_0) \sim p(\mathbf{x}, \mathbf{y}_0)$  ▷ sample from dataset
3:   if pretrain then ▷ pretrain on patch
4:      $(\mathbf{x}, \mathbf{y}_0) = \text{crop}(\mathbf{x}, \mathbf{y}_0)$ 
5:      $t \sim \text{Uniform}(0, T)$ ;  $\epsilon \sim \mathcal{N}(\mathbf{0}, \mathbf{I})$ 
6:     for  $i = 0, 1, \dots, b_2$  do
7:        $\hat{\mathbf{Y}}^{2D(a)}[:, i, :] \leftarrow \epsilon_{\theta_a}^{2D(a)}(\mathbf{y}_t[:, i, :], \mathbf{x}[:, i, :], t)$ 
8:     for  $j = 0, 1, \dots, b_3$  do
9:        $\hat{\mathbf{Y}}^{2D(b)}[:, :, j] \leftarrow \epsilon_{\theta_b}^{2D(b)}(\mathbf{y}_t[:, :, j], \mathbf{x}[:, :, j], t)$ 
10:    Take a gradient descent step on
11:     $\nabla_{\theta_{3D}} \|\epsilon_{\theta_{3D}}^{3D}(\mathbf{y}_t, \mathbf{x}, \hat{\mathbf{Y}}^{2D(a)}, \hat{\mathbf{Y}}^{2D(b)}, t) - \epsilon\|_2^2$ 
12:  until converged

```

Algorithm 2 Inference of Diff-Ensembler

```

1:  $(\mathbf{x}) \sim p(\mathbf{x})$  ▷ sample from dataset
2:  $\mathbf{y}_T \sim N(0, 1)$ 
3: for  $t = T, \dots, 1, 0$  do
4:   for  $i = 0, 1, \dots, b_2$  do
5:      $\hat{\mathbf{Y}}^{2D(a)}[:, i, :] \leftarrow \epsilon_{\theta_a}^{2D(a)}(\mathbf{y}_t[:, i, :], \mathbf{x}[:, i, :], t)$ 
6:   for  $j = 0, 1, \dots, b_3$  do
7:      $\hat{\mathbf{Y}}^{2D(b)}[:, :, j] \leftarrow \epsilon_{\theta_b}^{2D(b)}(\mathbf{y}_t[:, :, j], \mathbf{x}[:, :, j], t)$ 
8:    $\hat{\epsilon}^{3D} = \epsilon_{\theta}^{3D}(\mathbf{y}_t, \mathbf{x}, \hat{\mathbf{Y}}^{2D(a)}, \hat{\mathbf{Y}}^{2D(b)}, t)$ 
9:    $\hat{\mathbf{y}}_0 = \frac{\mathbf{y}_t - \sqrt{1 - \alpha_t} \hat{\epsilon}^{3D}}{\sqrt{\alpha_t}}$  ▷ get current estimation of  $\mathbf{y}_0$ 
10:  if Inverse problem then
11:     $\hat{\mathbf{y}}_0 \leftarrow \hat{\mathbf{y}}_0 - A^T(AA^T)^{-1}(A\hat{\mathbf{y}}_0 - \mathbf{x})$ 
12:   $\mathbf{y}_{t-1} = \sqrt{\alpha_{t-1}}\hat{\mathbf{y}}_0 + \sqrt{1 - \alpha_{t-1}}\epsilon$ 
13: return  $\mathbf{y}_0$ 

```

For training 2D models, we sliced the 3D volumes in two directions—transverse and sagittal planes for both TPDM baselines and Diff-Ensembler. In the super-resolution experiment, FLAIR images were downsampled using [4x4x4] average pooling. For modality translation, T1ce images served as inputs with FLAIR images as targets. Additionally, we investigated a multi-condition task, using both low-resolution FLAIR and T1ce images as input to predict high-resolution FLAIR images. In addition, this paper explores whether Diff-Ensembler can be generalized to different datasets. We apply Diff-Ensembler and related baselines in the super-resolution task in the FLAIR modality of the HCP dataset [10] to show that Diff-Ensembler is generalizable to various datasets. We show both quantitative and qualitative results in for HCP dataset in Sec. 10.

Baselines. We reproduced several baseline methods across a diverse set of established 2D and 3D translation models to ensure a comprehensive comparison. For slice-wise 2D models, we utilized Pix2pix [20] as the representative GAN-based method, U-Net [39] for supervised regression, Palette [41] as a diffusion-based approach, and I2SB [32] for optimal-translation-based modeling. Similarly, for 3D-based baselines, we used Pix2pix3D [20], U-Net3D [39], Med-DDPM [22] (or Palette3D). As stated in Sec. 1, Med-DDPM

uses a small denoising network and thus demonstrates limited performance. In addition, we used Palette-2.5D for another baseline, which uses multiple consecutive 2D slices as input. Several existing approaches closely related to our method combine multiple pre-trained 2D diffusion models in perpendicular orientations, demonstrating enhanced performance over other baselines. For instance, TPDM [27] combines two 2D diffusion models trained on perpendicular planes. To support modality translation, we adapted the TPDM’s 2D backbone to Palette [41] architecture in place for DPS [7]. Furthermore, TOSM [30] employs three perpendicularly trained 2D diffusion models, whereas MADM [4] uses three 2.5D diffusion models. We perform a hyper-parameter search on the super-resolution task on the BraTS dataset for all baselines.

Model Architecture and Variants. To make a fair comparison, we use pre-trained 2D models from TPDM, TOSM, and MADM utilizing an existing 3D diffusion model architecture, Med-DDPM [22]. The TPDM-based model is our main model as it is ~30% more efficient in inference speed and model size than the TOSM-based model, as shown in Tab. 8. Meanwhile, MADM-based and TOSM-based models are two heavier variants of our model that demonstrate performance gains in all metrics. Consistent performance improvement in all three variants demonstrates that our model can serve as a plug-in-and-play mechanism for multiple combinations of 2D/2.5D model backbones and existing 3D model architectures. We also include a more detailed model architecture in Sec. 11.

Metrics. We used multiple metrics to assess both the accuracy and realism of generated MRI images. For accuracy, we used peak signal-to-noise ratio (PSNR) and the structural similarity index measure (SSIM), both of which are widely used. To evaluate quality and realism, we used the maximum mean discrepancy (MMD) [14] and the Fréchet inception distance (FID) metrics [17]. Lower MMD/FID scores imply the generated images are more realistic. To evaluate the FID score, following common practice [11, 46], we adopted the same pre-trained model [3] to extract features and calculate the FID metrics in the feature space. In addition, since all diffusion-based models have uncertainty with different noise, we perform inference multiple times using different ϵ to produce a voxel-wise mean and standard deviation to calculate uncertainty awareness metrics. We show the uncertainty-aware quantitative and qualitative metrics in Sec. 8.

4.2. Experimental Results

We showcase the performance of Diff-Ensembler in solving various translation problems, including $4\times$ super-resolution, modality translation, and a fusion of both conditions in Fig. 3. We also include more randomly selected samples for more variants of our model in Sec. 9. Fig. 3 shows

the generation quality under various conditions and provides comparisons with other methods. The first two columns show the performance for super-resolution and modality translation, and the last columns show the model performance when fusing these two conditions. Our approach excels in faithfully recovering intricate high-frequency details, particularly in tumor-affected areas where such details are complex and often underrepresented. In the super-resolution task, from the zoomed-in panel, Diff-Ensembler clearly distinguishes tissue boundaries across various tissue types, including tumor and white/grey matter. In the modality translation task, the distribution of contrast difference between modalities is also better captured, as stated in Sec. 8. Furthermore, our method demonstrates superior volumetric consistency, while the baseline model exhibits noticeable artifacts. In the visualization of Diff-Ensembler, the fidelity of tissue texture and sharpness along all three orthogonal directions are well preserved, even though the 2D diffusion models in Diff-ensembl are trained only on transverse and sagittal planes. Our model reconstructs tumor regions with clearer margins, fewer artifacts, and higher resolution for samples containing tumors, providing superior performance in all three orthogonal directions. Overall, Diff-Ensembler generates images with higher accuracy, realism, and volumetric consistency. Tab. 1 summarizes the quantitative results of each translation task. Diff-Ensembler clearly surpasses other baseline models in most metrics, showing superior fidelity, structure, texture preservation, and noise suppression performance.

4.3. Downstream Task

We further evaluated the performance of Diff-Ensembler on a downstream task: tumor segmentation, where high-quality input modalities are crucial for accurately segmenting complex structures. Using the BraTS 2021 tumor segmentation dataset, we applied a pre-trained SwinUNetR [16] model with four modalities, replacing the ground-truth FLAIR modality with inferences from each model. Segmentation performance was assessed on Tumor Core (TC), Whole Tumor (WT), and Enhancing Tumor (ET) regions using two metrics: Dice score and Recovery rate. The Dice score measures segmentation quality, while the Recovery rate quantifies each model’s segmentation score recovered from low-quality FLAIR to the generated FLAIR, with segmentation using ground truth (GT) FLAIR as the upper bound and downsampled FLAIR as the lower bound. The Recovery rate is defined as:

$$\text{Recovery Rate} = \frac{\text{Prediction} - \text{Downsample}}{\text{Ground-Truth} - \text{Downsample}}$$

where **Prediction** refers to the segmentation performance using predicted FLAIR, **Downsample** is the performance with downsampled FLAIR, and **Ground Truth** is the performance with ground-truth FLAIR.

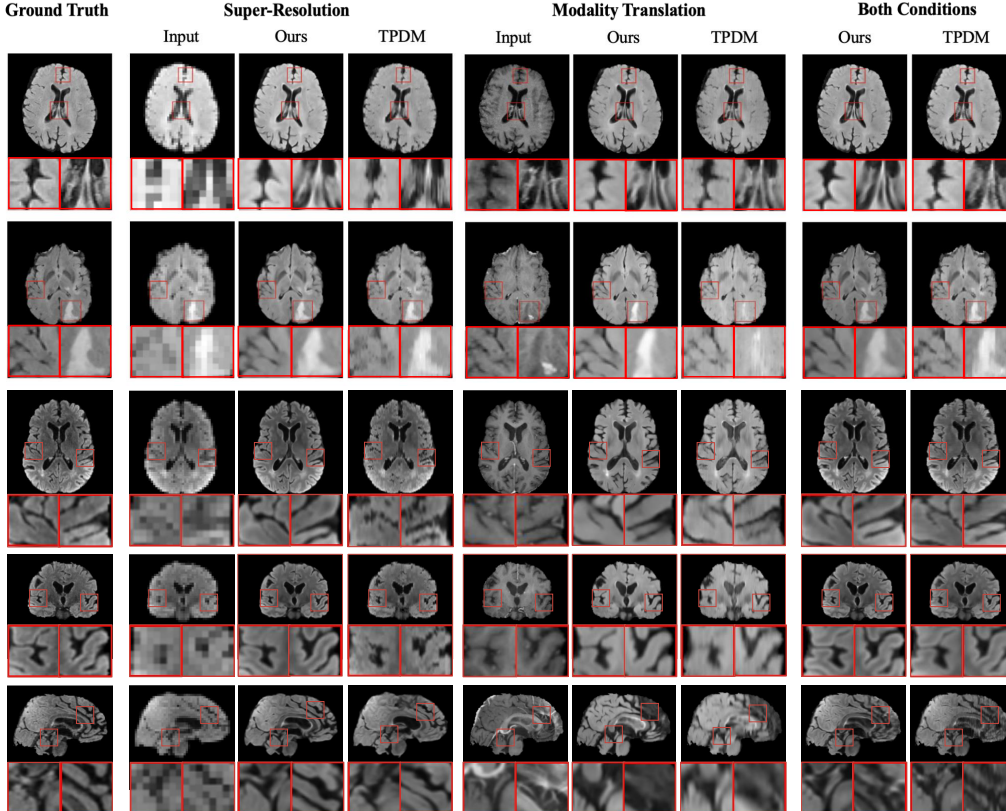


Figure 3. Visual comparison of generated samples for three different conditions. The first three rows show axial view slices from different MRI volumes. Neither Diff-Ensembler nor TPDM have a 2D model trained in this direction. The last three rows show slices for the same MRI volume in all three views. Diff-Ensembler reconstructs more realistic details with smoother edges and fewer artifacts.

Method	SR				MT				both condition			
	PSNR(\uparrow)	SSIM(\uparrow)	MMD(\downarrow)	FID($1e-4$)(\downarrow)	PSNR	SSIM	MMD	FID	PSNR	SSIM	MMD	FID
Pix2pix[20]	28.75	0.889	512.2	25.9	22.25	0.812	8989.0	577.6	31.78	0.923	133.9	11.8
U-net[39]	30.32	0.579	917.2	58.9	23.74	0.846	1829.0	320.3	33.58	0.931	83.5	36.6
Palette[41]	29.26	0.894	40.9	13.5	22.68	0.784	284.4	85.9	33.6	0.939	34.9	9.3
l2SB[32]	27.51	0.860	2644.5	47.7	20.75	0.738	35774.5	1343.6	31.3	0.905	1313.6	12.0
Palette-3D[41]	28.48	0.320	4222	88.7	Not Working				24.98	0.297	15926.0	463.1
Pix2pix-3D[20]	29.54	0.866	516.5	8.6	22.77	0.784	1974.0	342.2	31.86	0.900	87.81	56.2
U-net-3D[39]	31.23	0.892	115.6	59.6	23.43	0.809	487.5	273.8	32.95	0.922	43.3	43.9
Palette-2.5D[41]	29.76	0.834	35.37	12.3	23.04	0.728	1141.19	258.6	25.89	0.819	2858.37	138.92
TPDM[27]	32.23	0.922	29.35	17.3	25.35	0.868	176.3	185.5	35.12	0.945	14.5	22.2
Ours-TPDM	33.24	0.944	13.77	8.31	25.26	0.882	154.9	48.2	36.24	0.961	7.52	5.8
TOSM[30]	32.76	0.932	24.17	24.87	25.66	0.881	1018.91	209.5	35.44	0.947	8.32	14.53
Ours-TOSM	33.30	0.945	13.62	6.51	25.24	0.882	138.47	136.06	36.51	0.963	5.926	3.72
MADM[4]	33.02	0.946	30.92	35.64	25.47	0.874	1419.4	251.4	35.21	0.946	8.21	13.6
Ours-MADM	33.31	0.945	13.46	6.57	25.13	0.876	192.51	130.33	36.37	0.964	5.44	3.81

Table 1. Quantitative evaluation of Diff-Ensembler on BraTS dataset. Best metrics are highlighted in **bold**. The proposed model achieves better accuracy (PSNR/SSIM) given more 3D context than their corresponding variant in most tasks. More importantly, thanks to the introduced 3D representation, Diff-Ensembler achieves significantly better 3D realism (MMD/FID). We demonstrate the advantage of this 3D realism in downstream tasks in Sec. 4.3.

As shown in Tab. 2, our methods consistently outperformed other methods (see Section 14 for details).

Method	Dice (%)			Recovery (%)		
	TC	WT	ET	TC	WT	ET
GT FLAIR	82.71	89.17	81.20	-	-	-
Downsampled GT	82.30	86.82	80.30	-	-	-
SR						
TPDM	82.49	87.77	80.49	46.27	40.46	20.62
TOSM	82.52	87.21	80.80	54.55	16.51	55.28
ours-TPDM	82.69	87.85	80.94	93.71	43.80	71.69
ours-TOSM	82.59	87.86	80.87	70.14	44.38	63.94
MT						
TPDM	77.28	77.74	78.37	-	-	-
TOSM	77.94	79.21	78.64	-	-	-
ours-TPDM	77.88	78.51	78.22	-	-	-
ours-TOSM	78.84	78.73	79.52	-	-	-
both condition						
TPDM	82.45	87.69	80.74	36.31	37.25	49.28
TOSM	82.54	87.27	80.82	57.81	19.25	57.79
ours-TPDM	82.46	87.91	80.74	38.66	46.67	48.97
ours-TOSM	82.61	87.98	80.89	75.35	49.69	65.72

Table 2. Segmentation performance with the FLAIR modality replaced by model predictions. The recovery rate indicates the performance improvement achieved by replacing downsampled FLAIR with model-generated predictions.

Method	PSNR	SSIM	MMD	Training Time (GPU days)
TPDM	32.43	0.929	25.05	0
DiffEnsembler-small	35.34	0.956	8.64	4
DiffEnsembler	35.6	0.958	8.82	16
TPDM-both_cond	35.12	0.945	14.5	8
DiffEnsembler-both_cond	36.24	0.961	7.52	24

Table 3. Multi-modality fusion results for Diff-Ensembler. The models on both conditions (last 2 rows) show the metrics when re-training every 2D model on both conditions as in Tab. 1, representing an upper limit of multi-modality fusion performance. DiffEnsembler uses a 3D model to ensemble diffusion models conditioned on different input whereas TPDM uses a weighted average. DiffEnsembler-small uses a smaller model for the 3D model. All training experiments are performed on Nvidia RTX A100 GPU.

4.4. Multi-modality fusion

As discussed in Sec. 3.4, the Diff-Ensembler not only merges 2D models trained in different directions but also effectively integrates models pre-trained under various single conditions when faced with new combinations of input modalities given pre-trained 2D models on every single condition. We show the model’s performance in Tab. 3. Again, TPDM uses a weighted average for all 2D models, demonstrating limited performance. Using a 3D model of the original size, Diff-Ensembler provides a fusion scheme without re-training 2D models. Diff-Ensembler-small further improves training speed with marginal performance drop to flexibly support multi-modality fusion. This strategy resembles the mixture-of-experts model and could establish a foundational 3D model, capable of generating images that blend multiple conditions.

4.5. Ablation Studies

We provide an ablation study in Tab. 4 on the key design elements for Diff-Ensembler, which includes: (1) **Feature merging**: The 2D models not only contribute their outputs but also pass their feature maps to the 3D model. (2) **Fine-tune**: We initially pre-train the model on 3D patches and then fine-tune it on the full volume to speed up training. (3) **Consistency**: Inspired by DPS [7] and score-SDE [45], we implement self-consistency projections at each denoising step. All these designs show performance gain in the super-resolution task. In addition, we benchmark the smaller variant in Sec. 4.4 for comparison, which shows a moderate performance drop compared to our best model.

Smaller model	Consistency	Finetune	Feature	PSNR	SSIM	MMD
-	-	-	-	32.83	0.935	25.45
-	✓	-	-	32.88	0.94	18.84
-	✓	✓	-	32.97	0.941	15.24
-	✓	-	✓	33.04	0.942	17.76
-	✓	✓	✓	33.24	0.944	13.77
✓	✓	✓	-	32.8	0.937	16.78

Table 4. Ablation studies of additional design elements in Diff-Ensembler.

5. Conclusion

In this work, we have introduced Diff-Ensembler, an innovative hybrid model that integrates the strengths of both 2D and 3D diffusion models. By training multiple 2D diffusion models on orthogonal planes and fusing their outputs through a 3D ensemble model, Diff-Ensembler successfully overcomes the inherent limitations of each approach. Diff-Ensembler provides strong insights for diffusion model ensembling as the first work to adopt an MoE model in the score function space. Empirical evaluations on various 3D MRI image translation tasks, including super-resolution and modality translation, have shown that Diff-Ensembler achieves unmatched accuracy, realism, and volumetric consistency. In addition to computational and memory efficiency, the approach offers considerable flexibility in merging models conditioned on different domains.

Limitations Unlike some other multi-stage models [19, 58], Diff-Ensembler struggles with joint end-to-end training due to the substantial computational demands of simultaneously managing high-capacity 2D models and the volumetric complexities of 3D tasks. In addition, the model’s dependency on patchwise pre-training for efficient 3D model learning presents limitations for tasks requiring the integration of long-range spatial information, such as large-area inpainting and compressed sensing MRI. Therefore, Diff-Ensembler may require longer training for such tasks.

6. Acknowledgment

This work used the Delta system at the National Center for Supercomputing Applications through allocations CIS230243 and CIS240171 from the Advanced Cyberinfrastructure Coordination Ecosystem: Services & Support (ACCESS) program, which is supported by National Science Foundation grants #2138259, #2138286, #2138307, #2137603, and #2138296. We also thank Xiaoyue Li for the valuable discussion.

References

- [1] Mohamed Akrouf, Bálint Gyepesi, Péter Holló, Adrienn Poór, Blága Kincso, Stephen Solis, Katrina Cirone, Jeremy Kawahara, Dekker Slade, Latif Abid, et al. Diffusion-based data augmentation for skin disease classification: Impact across original medical datasets to fully synthetic images. In *International Conference on Medical Image Computing and Computer-Assisted Intervention*, pages 99–109. Springer, 2023. 1
- [2] Ujjwal Baid, Satyam Ghodasara, Suyash Mohan, Michel Bilello, Evan Calabrese, Errol Colak, Keyvan Farahani, Jayashree Kalpathy-Cramer, Felipe C Kitamura, Sarthak Pati, et al. The rsna-asnr-miccai brats 2021 benchmark on brain tumor segmentation and radiogenomic classification. *arXiv preprint arXiv:2107.02314*, 2021. 2, 5
- [3] Sihong Chen, Kai Ma, and Yefeng Zheng. Med3d: Transfer learning for 3d medical image analysis. *arXiv preprint arXiv:1904.00625*, 2019. 6
- [4] Tianqi Chen, Jun Hou, Yinchu Zhou, Huidong Xie, Xiongchao Chen, Qiong Liu, Xueqi Guo, Menghua Xia, James S. Duncan, Chi Liu, and Bo Zhou. 2.5d multi-view averaging diffusion model for 3d medical image translation: Application to low-count pet reconstruction with ct-less attenuation correction, 2024. 1, 2, 6, 7
- [5] Shin-I Cheng, Yu-Jie Chen, Wei-Chen Chiu, Hung-Yu Tseng, and Hsin-Ying Lee. Adaptively-realistic image generation from stroke and sketch with diffusion model. In *Proceedings of the IEEE/CVF Winter Conference on Applications of Computer Vision (WACV)*, pages 4054–4062, 2023. 3
- [6] Hyungjin Chung, Byeongsu Sim, Dohoon Ryu, and Jong Chul Ye. Improving diffusion models for inverse problems using manifold constraints, 2022. 2
- [7] Hyungjin Chung, Jeongsol Kim, Michael T. Mccann, Marc L. Klasky, and Jong Chul Ye. Diffusion posterior sampling for general noisy inverse problems, 2023. 3, 6, 8
- [8] Hyungjin Chung, Eun Sun Lee, and Jong Chul Ye. Mr image denoising and super-resolution using regularized reverse diffusion. *IEEE Transactions on Medical Imaging*, 42(4): 922–934, 2023. 1
- [9] Salman Ul Hassan Dar, Mahmut Yurt, Levent Karacan, Aykut Erdem, Erkut Erdem, and Tolga Çukur. Image synthesis in multi-contrast mri with conditional generative adversarial networks. *IEEE Transactions on Medical Imaging*, 38:2375–2388, 2018. 1
- [10] Van Essen DC, Smith SM, Barch DM, Behrens TE, Yacoub E, Ugurbil K, and WU-Minn HCP Consortium. The wu-minn human connectome project: an overview, 2013. 2, 5, 1
- [11] Zolnamar Dorjsembe, Hsing-Kuo Pao, Soddavilan Odonchimed, and Furen Xiao. Conditional diffusion models for semantic 3d brain mri synthesis. *IEEE Journal of Biomedical and Health Informatics*, 2024. 1, 2, 4, 6
- [12] Virginia Fernandez, Walter Hugo Lopez Pinaya, Pedro Borges, Petru-Daniel Tudosiu, Mark S Graham, Tom Vercauteren, and M Jorge Cardoso. Can segmentation models be trained with fully synthetically generated data? In *International Workshop on Simulation and Synthesis in Medical Imaging*, pages 79–90. Springer, 2022. 1
- [13] Norma Latif Fitriyani, Muhammad Syafrudin, Ganjar Alfian, and Jongtae Rhee. Development of disease prediction model based on ensemble learning approach for diabetes and hypertension. *Ieee Access*, 7:144777–144789, 2019. 3
- [14] Arthur Gretton, Karsten M Borgwardt, Malte J Rasch, Bernhard Schölkopf, and Alexander Smola. A kernel two-sample test. *The Journal of Machine Learning Research*, 13(1):723–773, 2012. 6
- [15] Bin Dong Hai-Miao Zhang. A review on deep learning in medical image reconstruction. *Journal of the Operations Research Society of China*, 8(2):311, 2020. 1
- [16] Ali Hatamizadeh, Vishwesh Nath, Yucheng Tang, Dong Yang, Holger Roth, and Daguang Xu. Swin unetr: Swin transformers for semantic segmentation of brain tumors in mri images, 2022. 1, 3, 6, 4
- [17] Martin Heusel, Hubert Ramsauer, Thomas Unterthiner, Bernhard Nessler, and Sepp Hochreiter. Gans trained by a two time-scale update rule converge to a local nash equilibrium. *Advances in neural information processing systems*, 30, 2017. 6
- [18] Jonathan Ho, Ajay Jain, and Pieter Abbeel. Denoising diffusion probabilistic models, 2020. 3
- [19] Ziqi Huang, Kelvin C. K. Chan, Yuming Jiang, and Ziwei Liu. Collaborative diffusion for multi-modal face generation and editing, 2023. 3, 8
- [20] Phillip Isola, Jun-Yan Zhu, Tinghui Zhou, and Alexei A Efros. Image-to-image translation with conditional adversarial networks. In *Proceedings of the IEEE conference on computer vision and pattern recognition*, pages 1125–1134, 2017. 5, 7
- [21] Albert Q. Jiang, Alexandre Sablayrolles, Antoine Roux, Arthur Mensch, Blanche Savary, Chris Bamford, Devendra Singh Chaplot, Diego de las Casas, Emma Bou Hanna, Florian Bressand, Gianna Lengyel, Guillaume Bour, Guillaume Lample, Léo Renard Lavaud, Lucile Saulnier, Marie-Anne Lachaux, Pierre Stock, Sandeep Subramanian, Sophia Yang, Szymon Antoniak, Teven Le Scao, Théophile Gervet, Thibaut Lavril, Thomas Wang, Timothée Lacroix, and William El Sayed. Mixtral of experts, 2024. 3
- [22] Euijin Jung, Miguel Luna, and Sang Hyun Park. Conditional gan with 3d discriminator for mri generation of alzheimer’s disease progression. *Pattern Recognition*, 133:109061, 2023. 5, 6
- [23] Yassaman Kazemi and Seyed Abolghasem Mirroshandel. A novel method for predicting kidney stone type using ensemble learning. *Artificial intelligence in medicine*, 84:117–126, 2018. 3

- [24] Hammernik Kerstin, Klatzer Teresa, Kobler Erich, Recht Michael P., Sodickson Daniel K., Pock Thomas, and Knoll Florian. Learning a variational network for reconstruction of accelerated mri data. *Magnetic Resonance in Medicine*, 79(6):3055–3071. 1
- [25] Firas Khader, Gustav Müller-Franzes, Soroosh Tayebi Arasteh, Tianyu Han, Christoph Haarbuerger, Maximilian Schulze-Hagen, Philipp Schad, Sandy Engelhardt, Bettina Baeßler, Sebastian Foersch, et al. Denoising diffusion probabilistic models for 3d medical image generation. *Scientific Reports*, 13(1):7303, 2023. 2
- [26] Volodymyr Kuleshov, Nathan Fenner, and Stefano Ermon. Accurate uncertainties for deep learning using calibrated regression, 2018. 1
- [27] Suhyeon Lee, Hyungjin Chung, Minyoung Park, Jonghyuk Park, Wi-Sun Ryu, and Jong Chul Ye. Improving 3d imaging with pre-trained perpendicular 2d diffusion models. In *Proceedings of the IEEE/CVF International Conference on Computer Vision*, pages 10710–10720, 2023. 1, 2, 3, 6, 7
- [28] Amaury Leroy, Kumar Shreshtha, Marvin Lerousseau, Théophraste Henry, Théo Estienne, Marion Classe, Nikos Paragios, Vincent Grégoire, and Eric Deutsch. Magnetic resonance imaging virtual histopathology from weakly paired data. In *Proceedings of the MICCAI Workshop on Computational Pathology*, pages 140–150. PMLR, 2021. 1
- [29] Xiaoyue Li, Kai Shang, Gaoang Wang, and Mark D Butala. Ddmm-synth: A denoising diffusion model for cross-modal medical image synthesis with sparse-view measurement embedding. *arXiv preprint arXiv:2303.15770*, 2023. 5
- [30] Zirong Li, Yanyang Wang, Jianjia Zhang, Weiwen Wu, and Hengyong Yu. Two-and-a-half order score-based model for solving 3d ill-posed inverse problems. *Computers in Biology and Medicine*, 168:107819, 2024. 2, 6, 7
- [31] Dong Liang, Jing Cheng, Ke Ziwen, and Lei Ying. Deep magnetic resonance image reconstruction: Inverse problems meet neural networks. *IEEE Signal Processing Magazine*, 37: 141–151, 2020. 1
- [32] Guan-Hong Liu, Arash Vahdat, De-An Huang, Evangelos A Theodorou, Weili Nie, and Anima Anandkumar. I²sb: Image-to-image schrödinger bridge. *ICML*, 2023. 5, 7
- [33] Haotian Liu, Chunyuan Li, Qingyang Wu, and Yong Jae Lee. Visual instruction tuning, 2023. 4
- [34] Yanbin Liu, Girish Dwivedi, Farid Boussaid, Frank Sanfilippo, Makoto Yamada, and Mohammed Bennamoun. Inflating 2d convolution weights for efficient generation of 3d medical images. *Computer Methods and Programs in Biomedicine*, 240:107685, 2023. 2
- [35] Qing Lyu, Hongming Shan, and Ge Wang. Mri super-resolution with ensemble learning and complementary priors. *IEEE Transactions on Computational Imaging*, 6:615–624, 2020. 1
- [36] Morteza Mardani, Enhao Gong, Joseph Y Cheng, Shreyas Vasanawala, Greg Zaharchuk, Marcus Alley, Neil Thakur, Song Han, William Dally, John M Pauly, et al. Deep generative adversarial networks for compressed sensing automates mri. *IEEE Trans Med Imaging*, 2019. 1
- [37] Ziyu Meng, Rong Guo, Yudu Li, Yue Guan, Tianyao Wang, Yibo Zhao, Brad Sutton, Yao Li, and Zhi-Pei Liang. Accelerating t2 mapping of the brain by integrating deep learning priors with low-rank and sparse modeling. *Magnetic Resonance in Medicine*, 85(3):1455–1467, 2021. Publisher Copyright: © 2020 International Society for Magnetic Resonance in Medicine Copyright: Copyright 2020 Elsevier B.V., All rights reserved. 1
- [38] Wei Peng, Ehsan Adeli, Tomas Bosschieter, Sang Hyun Park, Qingyu Zhao, and Kilian M Pohl. Generating realistic brain mris via a conditional diffusion probabilistic model. In *International Conference on Medical Image Computing and Computer-Assisted Intervention*, pages 14–24. Springer, 2023. 2
- [39] Olaf Ronneberger, Philipp Fischer, and Thomas Brox. U-net: Convolutional networks for biomedical image segmentation, 2015. 5, 7
- [40] Chitwan Saharia, Jonathan Ho, William Chan, Tim Salimans, David J. Fleet, and Mohammad Norouzi. Image super-resolution via iterative refinement, 2021. 2, 3, 4, 1
- [41] Chitwan Saharia, William Chan, Huiwen Chang, Chris Lee, Jonathan Ho, Tim Salimans, David Fleet, and Mohammad Norouzi. Palette: Image-to-image diffusion models. In *ACM SIGGRAPH 2022 conference proceedings*, pages 1–10, 2022. 2, 3, 5, 6, 7
- [42] Zenglin Shi, Pascal Mettes, Guoyan Zheng, and Cees Snoek. Frequency-supervised mr-to-ct image synthesis. In *Deep Generative Models, and Data Augmentation, Labelling, and Imperfections: First Workshop, DGM4MICCAI 2021, and First Workshop, DALI 2021, Held in Conjunction with MICCAI 2021, Strasbourg, France, October 1, 2021, Proceedings I*, pages 3–13. Springer, 2021. 1
- [43] Bowen Song, Soo Min Kwon, Zecheng Zhang, Xinyu Hu, Qing Qu, and Liyue Shen. Solving inverse problems with latent diffusion models via hard data consistency. *ICLR*, 2024. 3
- [44] Yang Song, Conor Durkan, Iain Murray, and Stefano Ermon. Maximum likelihood training of score-based diffusion models, 2021. 2
- [45] Yang Song, Liyue Shen, Lei Xing, and Stefano Ermon. Solving inverse problems in medical imaging with score-based generative models, 2022. 3, 8
- [46] Li Sun, Junxiang Chen, Yanwu Xu, Mingming Gong, Ke Yu, and Kayhan Batmanghelich. Hierarchical amortized gan for 3d high resolution medical image synthesis. *IEEE journal of biomedical and health informatics*, 26(8):3966–3975, 2022. 6
- [47] Hristina Uzunova, Jan Ehrhardt, and Heinz Handels. Memory-efficient gan-based domain translation of high resolution 3d medical images. *Computerized Medical Imaging and Graphics*, 86:101801, 2020. 2
- [48] Sanketh Vedula, Ortal Senouf, Alex M Bronstein, Oleg V Michailovich, and Michael Zibulevsky. Towards ct-quality ultrasound imaging using deep learning. *arXiv preprint arXiv:1710.06304*, 2017. 1
- [49] Ge Wang, Jong Chul Ye, and Bruno De Man. Deep learning for tomographic image reconstruction. *Nature Machine Intelligence*, 2:737–748, 2020. 1

- [50] Zhendong Wang, Yifan Jiang, Huangjie Zheng, Peihao Wang, Pengcheng He, Zhangyang Wang, Weizhu Chen, and Mingyuan Zhou. Patch diffusion: Faster and more data-efficient training of diffusion models, 2023. [4](#)
- [51] Jelmer M Wolterink, Anna M Dinkla, Mark HF Savenije, Peter R Seevinck, Cornelis AT van den Berg, and Ivana Išgum. Deep mr to ct synthesis using unpaired data. In *Simulation and Synthesis in Medical Imaging: Second International Workshop, SASHIMI 2017, Held in Conjunction with MICCAI 2017, Québec City, QC, Canada, September 10, 2017, Proceedings 2*, pages 14–23. Springer, 2017. [1](#)
- [52] Zhengshi Yang, Xiaowei Zhuang, Karthik Sreenivasan, Virendra Mishra, Tim Curran, and Dietmar Cordes. A robust deep neural network for denoising task-based fmri data: An application to working memory and episodic memory. *Medical Image Analysis*, 60:101622, 2019. [1](#)
- [53] Huixian Zhang, Hailong Li, Jonathan Dillman, Nehal Parikh, and Lili He. Multi-contrast mri image synthesis using switchable cycle-consistent generative adversarial networks. *Diagnostics*, 12:816, 2022. [1](#)
- [54] Lvmin Zhang, Anyi Rao, and Maneesh Agrawala. Adding conditional control to text-to-image diffusion models, 2023. [5](#)
- [55] Chenhong Zhou, Shengcong Chen, Changxing Ding, and Dacheng Tao. Learning contextual and attentive information for brain tumor segmentation. In *Brainlesion: Glioma, Multiple Sclerosis, Stroke and Traumatic Brain Injuries: 4th International Workshop, BrainLes 2018, Held in Conjunction with MICCAI 2018, Granada, Spain, September 16, 2018, Revised Selected Papers, Part II 4*, pages 497–507. Springer, 2019. [3](#)
- [56] Lingting Zhu, Zeyue Xue, Zhenchao Jin, Xian Liu, Jingzhen He, Ziwei Liu, and Lequan Yu. Make-a-volume: Leveraging latent diffusion models for cross-modality 3d brain mri synthesis, 2023. [2](#)
- [57] Lingting Zhu, Noel Codella, Dongdong Chen, Zhenchao Jin, Lu Yuan, and Lequan Yu. Generative enhancement for 3d medical images. *arXiv preprint arXiv:2403.12852*, 2024. [2](#)
- [58] Xiyue Zhu, Vlas Zyrianov, Zhijian Liu, and Shenlong Wang. Mapprior: Bird’s-eye view map layout estimation with generative models, 2023. [8](#)

Diff-Ensembler: Learning to Ensemble 2D Diffusion Models for Volume-to-Volume Medical Image Translation

Supplementary Material

7. Overview

In this supplementary material, we first discuss the uncertainty awareness results performed by our model and baselines by running the inference multiple times in Sec. 8. We provide more randomly selected results (We do exclude samples with low-quality GT) for more baselines and our variants in Sec. 9. Then, we provide our super-resolution result in an additional dataset, HCP dataset [10] in Sec. 10. We also provide more details on training and inference, including a detailed model architecture in Sec. 11 and training/inference speed in Sec. 12. We finally introduce a more detailed method for self-consistency projection in Sec. 13 and downstream task results in Sec. 14.

8. Uncertainty Awareness

As with most diffusion-based models, our models and some of our baselines can have uncertainty estimations. To study this uncertainty, we perform inference five times for each sample in our validation set. This gives us 5 PSNR and SSIM values for each data sample. We then calculate the standard deviation (std) of the PSNR and SSIM for each sample and include the mean std across the entire validation set in Tab. 5. This further validates that our performance boost in PSNR and SSIM is significant. For the main variant, TPDM and Ours-TPDM, in the super-resolution task, we have a 1.01 boost in PSNR, which is much larger than the std of PSNR for both models (0.0066 and 0.0298). Even for MADM and Ours-MADM, where we have the most marginal PSNR boost, the boost is still 0.3, around 10 times larger than the std for both models (0.0308 and 0.0276). In contrast, in modality translation, the std is significantly larger since the uncertainty in this task is much larger than in others, indicating the PSNR drop is not as significant. In fact, previous work [40] argues that PSNR prefers blurry results, and highly diverse and realistic results typically have low PSNR in tasks with high uncertainty.

In addition, this inference also provides a mean μ_i and std estimation σ_i for each voxel. We use Mean Absolute Calibration Error (MACE) [26] to measure the uncertainty awareness of our model and baseline. MACE measures the absolute difference between the predicted uncertainty and the actual error, as shown in Eq. 7.

$$\text{MACE} = \frac{1}{N} \sum_{i=1}^N |\sigma_i - |y_i - \mu_i|| \quad (7)$$

As demonstrated in Table 5, all variants of our model

exhibit lower MACE values compared to their respective baselines. This indicates that the standard deviation (std) predicted by our model, derived from multiple inferences, provides a more accurate estimation of the true error relative to the ground truth. Consequently, our model exhibits improved uncertainty awareness. For qualitative results in uncertainty awareness, we demonstrate our model’s results with the uncertainty map and error map across various tasks and variants in Fig. 14 15 16 17 18 19 20 21. As shown in the figures, the uncertainty map aligns well with the actual error map, demonstrating decent uncertainty awareness for all models. Notably, our model usually has a higher uncertainty in modality translation tasks in Fig. 16 and 17. In the modality translation task, the $p(\mathbf{y}|\mathbf{x})$ should have a high variance in overall contrast. Our model outputs samples that are highly diverse in overall contrast, indicating that Diff-Ensembler is able to model the target 3D conditional distribution $p(\mathbf{y}|\mathbf{x})$ better. In contrast, our baselines tend to output the mean estimation for overall contrast, demonstrating higher PSNR but limited capability of generating diverse and realistic results.

9. Additional qualitative result

We show results for the variants that show the best metrics. Namely, we show results for MADM and Ours-MADM in the super-resolution task in Fig. 14 and 15, and show results for TOSM and Ours-TOSM for the other two tasks in Fig. 18 19 16 and 17. We include more samples in all 3 views in Fig. 20 and Fig. 21 in super-resolution tasks in addition to Fig. 3. Each figure contains 2 sample volumes, each of which contains visualizations in all three views in three rows. We show all results with uncertainty and error maps.

Similarly to Fig. 3, we find that both MADM and TOSM demonstrate similar artifacts as TPDM in high-frequency details due to a direct averaging in the score function. In contrast, Diff-Ensembler consistently demonstrates better 3D consistency and realism across all views by introducing pixel-space 3D representation and networks to replace the weighted averaging in the score function space. For example, in the 6-th row of Fig. 14 16, and 18, the results from baselines are blurry at the top left part of the brain, whereas Diff-Ensembler shows more smooth and consistent results.

Method	SR			MT			both condition		
	PSNR(\uparrow)	SSIM(\uparrow)	MACE($1e-4$)(\downarrow)	PSNR	SSIM	MACE	PSNR	SSIM	MACE
TPDM[27]	32.23 ± 0.0066	0.922 ± 0.000300	53.16	25.35 ± 0.2363	0.868 ± 0.00112	279.3	35.12 ± 0.0154	0.945 ± 0.00056	48.72
Ours-TPDM	33.24 ± 0.0298	0.944 ± 0.000261	44.63	25.26 ± 0.664	0.882 ± 0.00357	268.3	36.24 ± 0.0389	0.961 ± 0.000249	38.49
TOSM[30]	32.76 ± 0.02157	0.932 ± 0.000434	51.68	25.66 ± 0.2703	0.881 ± 0.00132	221.7	35.44 ± 0.0173	0.947 ± 0.00073	46.32
Ours-TOSM	33.30 ± 0.0296	0.945 ± 0.000240	42.89	25.24 ± 0.668	0.882 ± 0.00317	200.8	36.51 ± 0.0364	0.963 ± 0.000210	36.67
MADM[4]	33.02 ± 0.0276	0.946 ± 0.000436	83.20	25.47 ± 0.2573	0.874 ± 0.00143	251.4	35.21 ± 0.0165	0.946 ± 0.00063	47.89
Ours-MADM	33.31 ± 0.0308	0.945 ± 0.000278	42.03	25.13 ± 0.667	0.876 ± 0.00342	234.6	36.37 ± 0.0379	0.964 ± 0.00226	37.15

Table 5. Quantitative evaluation of Diff-Ensembler on BraTS dataset with uncertainty metrics. Our models’ performance boost is significant, given low standard deviations. Our model can also estimate uncertainty better through the standard deviation obtained by inference multiple times.

10. Result on HCP dataset

We present our super-resolution results on the FLAIR modality in the HCP [10] dataset to show our model is generalizable across datasets. The HCP dataset consists of 1251 MRI volumes with a resolution of $192 \times 152 \times 152$. In contrast to the BraTs dataset, HCP comprises healthy brains with no brain tumors. Experiments results in Tab. 6 show that our model shows around 1.5 performance boost in PSNR. We also present the qualitative results in Fig. 4, including all 3 views. Again, Diff-Ensembler shows better 3D consistency and realism. For example, in the top-right part in the third view, our baseline demonstrates jittering and artifacts, while our model produces more realistic detail and smoother edges.

Method	PSNR	SSIM	MMD	FID($1e-4$)
TPDM	28.17	0.890	81.81	35.70
Ours-TPDM	29.62	0.914	67.96	22.12

Table 6. Super-resolution result in HCP dataset.

11. Detailed model architecture

In this section, we show detailed model architecture for 2D, 3D, and the smaller variant of the 3D model in Tab. 9, Tab. 10, and Tab. 11, respectively. In addition, we show other related hyper-parameters in Tab. 7. We modified the architecture of the 2D diffusion model from Palette [41] and the 3D models from med-ddpm [11].

Given the differences in problem setting and dataset between our work and that of Palette, we conduct a comprehensive hyper-parameter search based on the super-resolution

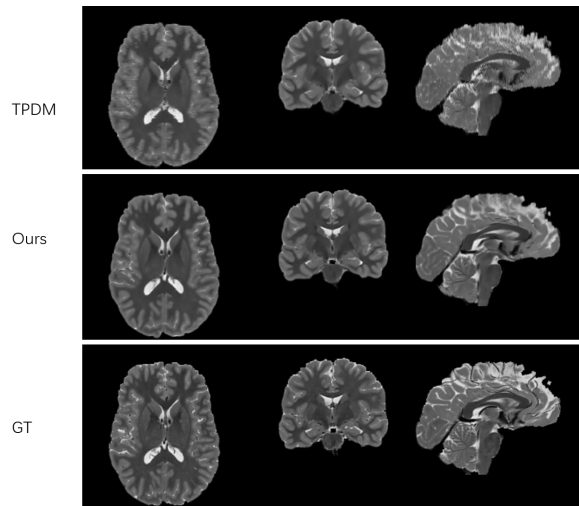


Figure 4. Qualitative results in HCP dataset. The input is a $4 \times 4 \times 4$ downsampled version of the ground truth.

tasks. This search explores various configurations, including the number of channels, transformer layers, and learning rate, among others. The hyper-parameter search is conducted to optimize the performance of our baseline models, Palette2D, Palette3D, and Palette2.5D, in Tab. 1. While such a search could potentially enhance the performance of our proposed model, we do not perform a hyper-parameter search to optimize the performance of Diff-Ensembler, TPDM, TOSM, and MADM. This practice ensures a fair comparison between our model and their corresponding baselines, TPDM, TOSM, and MADM. Moreover, this shows that our model can be a plug-in-and-play mechanism for existing pre-trained 2D and 3D model architecture.

Table 7. Other hyper-parameters

Parameter	2D Network	3D Network
Batch size	4	1
Diffusion steps	1000	1000
Inference steps (DDIM)	50	50
Noise scheduler	Linear	Linear
Learning rate	0.00005	0.0001
Optimizer	Adam	Adam

12. Training and inference speed

We present training inference speed in Tab. 8. All experiments are done with RTX A100-40GB GPU. Since Diff-Ensembler needs to train an additional model on top of the baselines, our training time is inevitably higher. We need 16 GPU days to train our 3D models, which results in a 16-day increase in training time for most model variants compared to their corresponding baselines. Our models are also relatively slower in inference since we need to perform inference for an additional 3D model. However, as mentioned in Sec. 1, the 3D model is naturally limited in size due to computational challenges in training. Therefore, 3D inference is more efficient than slice-wise 2D inference. As a result, the increase in inference time is significantly smaller than in training. As shown in Tab. 8, our 3D model is around 30% faster than one 2D model and, therefore, leads to a 36% increase in inference time for Ours-TPDM and 26% for Ours-MADM and Ours-MADM.

Moreover, we find that the TPDM-based models are significantly faster than other variants of the models. Given the advantage of computational efficiency, we use TPDM and Ours-TPDM as our main variables for the model and the baseline. Furthermore, to perform a more complete ablation study, the smaller 3D model decreases the inference and training time of the 3D model by 75% while showing a consistent performance boost over TPDM and a moderate performance drop compared to Ours-TPDM as shown in Tab. 1.

13. Details for consistency projection

In this section, we provide the exact definition and detail for self-consistency projection mentioned in Sec. 3.1. In this work, we address the inverse problem using a diffusion model with consistency projections. The goal is to recover a high-resolution image, \mathbf{y} , from its low-resolution observation \mathbf{x} , which is obtained through a linear degradation process. Specifically, the degradation process is modeled as: $\mathbf{x} = A\mathbf{y}$.

In the 3D case, the degradation operator A represents a downsampling operation that reduces the resolution of a volume \mathbf{y} by a factor of 4 along each spatial dimension

Table 8. Training and Inference time for each model, GPUs are A100 with 40G memory.

Time	Training time (GPU days)	Inference time (minutes per volume)
2D Palette	8	0.85
2D I2SB	5	4.58
3D Pix2pix	6	0.0398
3D Unet	6	0.0398
3D Palette	12	0.6
TPDM	16	1.72
Ours-TPDM	32	2.34
Ours-TPDM-small	20	1.92
TOSM	24	2.55
Ours-MADM	40	3.23
MADM	36	2.76
Ours-MADM	52	3.56

(x , y and z) and resizes it back to the original resolution. This means that each voxel in the low-resolution volume \mathbf{x} corresponds to the average of a $[4 \times 4 \times 4]$ region in the high-resolution volume \mathbf{y} . Specifically, let $\mathbf{y}, \mathbf{x} \in \mathbb{R}^{b_1 \times b_2 \times b_3}$. The operator matrix $A \in \mathbb{R}^{b_1 \times b_2 \times b_3, b_1 \times b_2 \times b_3}$ downscales the high-resolution volume \mathbf{y} into the low-resolution volume \mathbf{x} by averaging over $[4 \times 4 \times 4]$ blocks of voxel of \mathbf{y} . Therefore, A is a sparse matrix where each non-zero entry corresponds to the average of a block of $[4 \times 4 \times 4]$ voxels in \mathbf{y} being averaged to form a block of voxel in \mathbf{x} . Therefore, A is $\frac{1}{64}$ for the places where \mathbf{x} and \mathbf{y} belong to the same block, and A would be 0 elsewhere:

$$A[(i, j, k), (p, q, r)] = \begin{cases} \frac{1}{64} & \text{if } \mathbf{x}(i, j, k), \mathbf{y}(p, q, r) \in \text{block} \\ 0 & \text{Otherwise} \end{cases} \quad (8)$$

Since we are doing average over $[4 \times 4 \times 4]$, $\mathbf{x}(i, j, k)$ and $\mathbf{y}(p, q, r)$ are in the same block if and only if $i//4 == p//4$, $j//4 == q//4$, and $k//4 == r//4$.

In our diffusion process, we use $\hat{\mathbf{y}}_0(t) \leftarrow \hat{\mathbf{y}}_0(t) - A^T(AA^T)^{-1}(A\hat{\mathbf{y}}_0(t) - \mathbf{x})$ to make every of our mean prediction of $\hat{\mathbf{y}}_0$ a plausible estimation with $\mathbf{x} = A\hat{\mathbf{y}}_0(t)$

To compute matrix multiplication more efficiently in a super-resolution setting, we actually use $\hat{\mathbf{y}}_0(t) \leftarrow \hat{\mathbf{y}}_0(t) - (A\hat{\mathbf{y}}_0(t) - \mathbf{x})$ in our code. This works in the average pooling downsample because $AA\mathbf{y} = A\mathbf{y}$ since A represents the degradation process composed of average pooling followed by resizing the image back to its original resolution.

14. Details in downstream task

In Section 4.3, we evaluate tumor segmentation performance using three types of FLAIR inputs: the ground truth FLAIR modality, 4x downsampled FLAIR modality (as de-

scribed in Section 4.1), and the 4x super-resolution FLAIR prediction on the downsampled FLAIR. Accurate tumor segmentation is crucial in medical imaging, and its performance heavily relies on the quality of the input data. It requires High-quality inputs for precise localization and delineation of tumor boundaries, while, depending on its degradation level, the degraded inputs could significantly lower segmentation accuracy and reliability. We use a robust pre-trained segmentation model, SwinUNet [16], which takes four modalities (T1, T1ce, T2, and FLAIR) as input. For this downstream task, our objective is to assess how well the models can recover segmentation performance when working with degraded inputs. Segmentation is performed with other modalities with ground truth inputs and a FLAIR input from the ground truth FLAIR, downsampled FLAIR, or the model-predicted FLAIR. Note that because there is no degraded FLAIR modality available in the modality translation task, only dice scores are reported. For other tasks, including the super-resolution and both condition tasks, performance is measured using two metrics: (1) **Dice Score**, the primary metric of the segmentation model, and (2) **Recovery Rate**, a measure of how well model predictions improve upon degraded FLAIR inputs. The recovery rate is calculated as:

$$\text{Recovery Rate} = \frac{\text{Prediction} - \text{Downsample}}{\text{Ground Truth} - \text{Downsample}}$$

where **Prediction** refers to the segmentation performance using predicted FLAIR, **Downsample** is the performance with downsampled FLAIR, and **Ground Truth** is the performance with ground truth FLAIR.

Fig. 5, 6, 7 illustrate the Dice score and Recovery rate comparisons across tumor categories. Dashed lines represent the lower and upper bounds. They show that segmentation performance with the predicted FLAIR modality from Diff-Ensembler-based models outperforms other methods, as Diff-Ensembler-based models are constantly positioned higher than others.

We also show qualitative results in the tumor segmentation task, on TPDm, TOSM, and Diff-Ensembler built based on these two models. Fig 8 and Fig 9 show the results in super-resolution, Fig 10 and Fig 11 show the results in modality translation, and Fig 12 and Fig 13 show the results given both conditions. In Fig 8, 13, 12, and 13, in the sagittal plane, we can observe that our models help segmentation model capture a branch coming out of the whole tumor, indicated by a red bounding box. This branch is only partially captured or entirely missed in predictions from other models. This shows that our model yields more precise predictions, allowing the tumor segmentation model to delineate the entire tumor boundary more accurately.

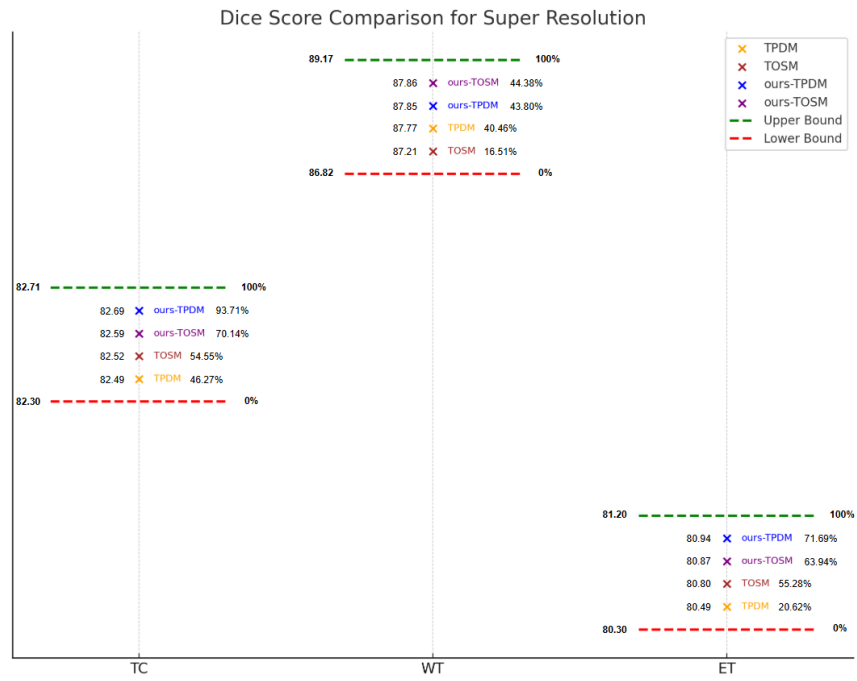


Figure 5. Comparison of Dice scores and recovery rates for super-resolution. The value on the left represents the Dice score, while the value on the right represents the recovery rate.

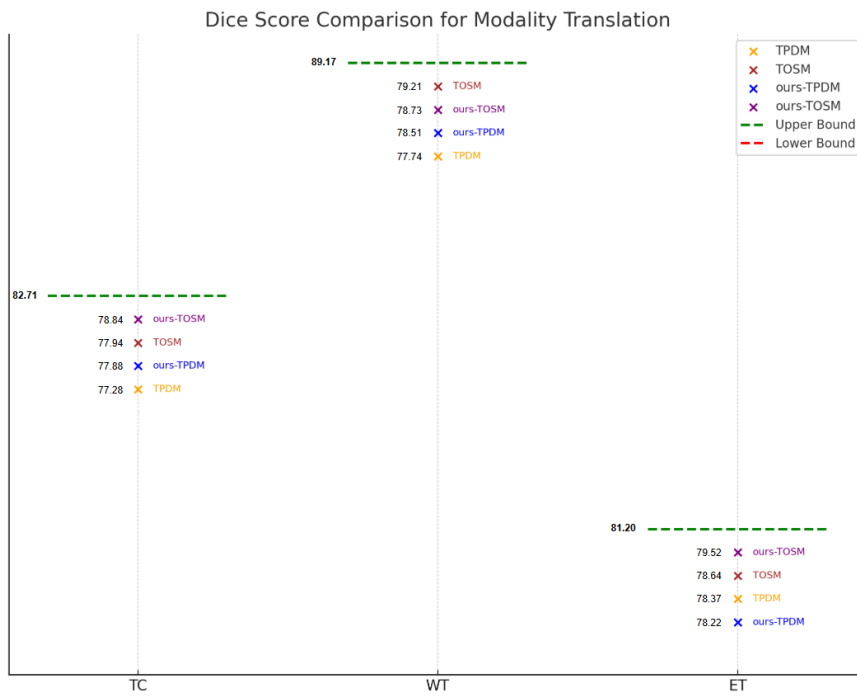


Figure 6. Comparison of Dice scores and recovery rates for modality translation. The value on the left represents the Dice score.

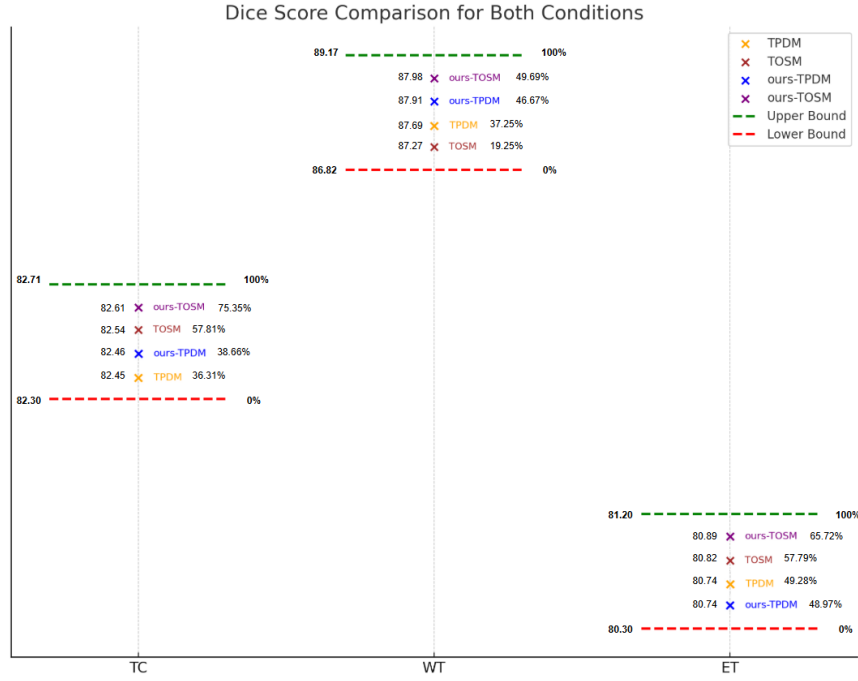


Figure 7. Comparison of Dice scores and recovery rates for both conditions. The value on the left represents the Dice score, while the value on the right represents the recovery rate.

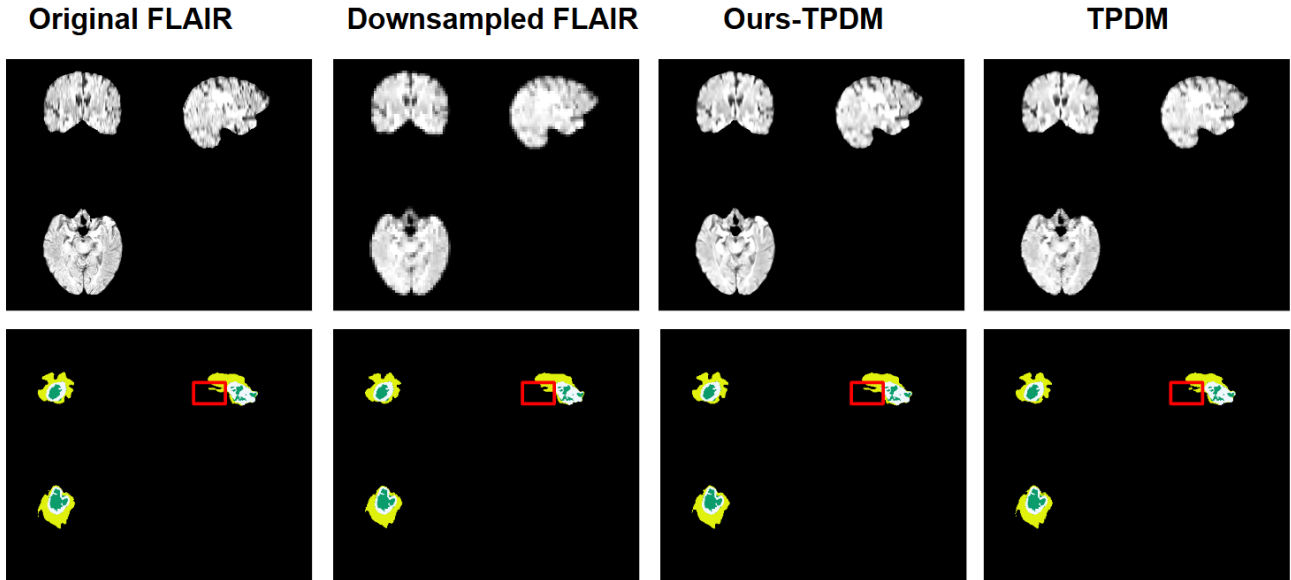


Figure 8. Qualitative results for the downstream task, tumor segmentation, in super-resolution task.

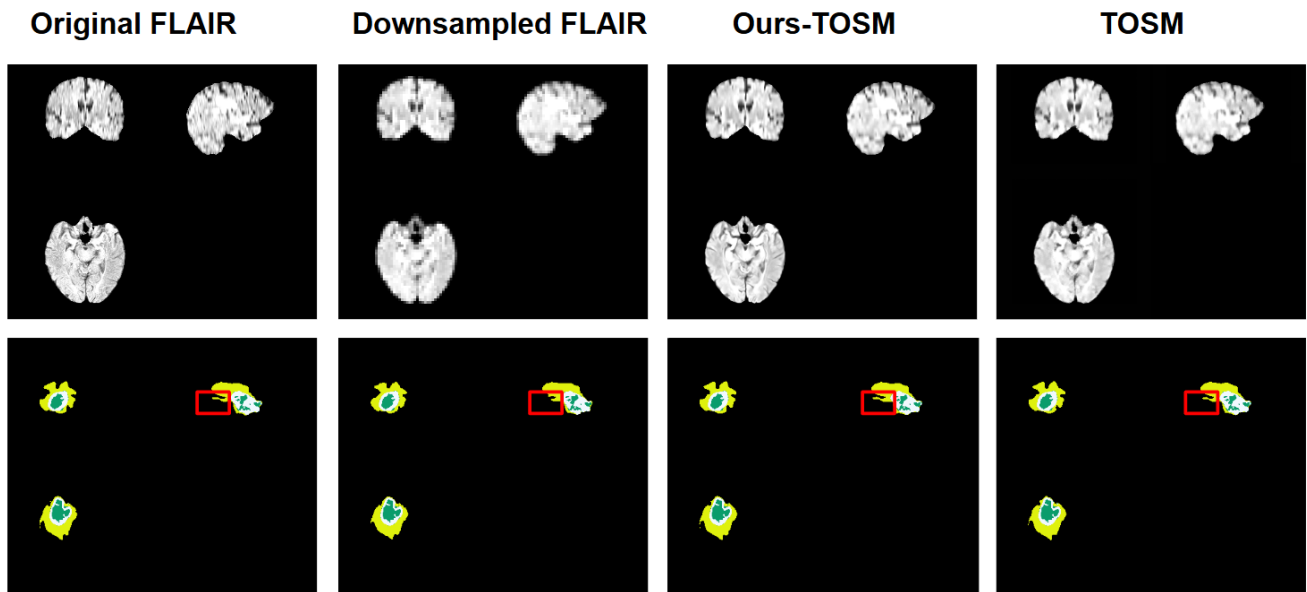


Figure 9. Qualitative results for the downstream task, tumor segmentation, in super-resolution task

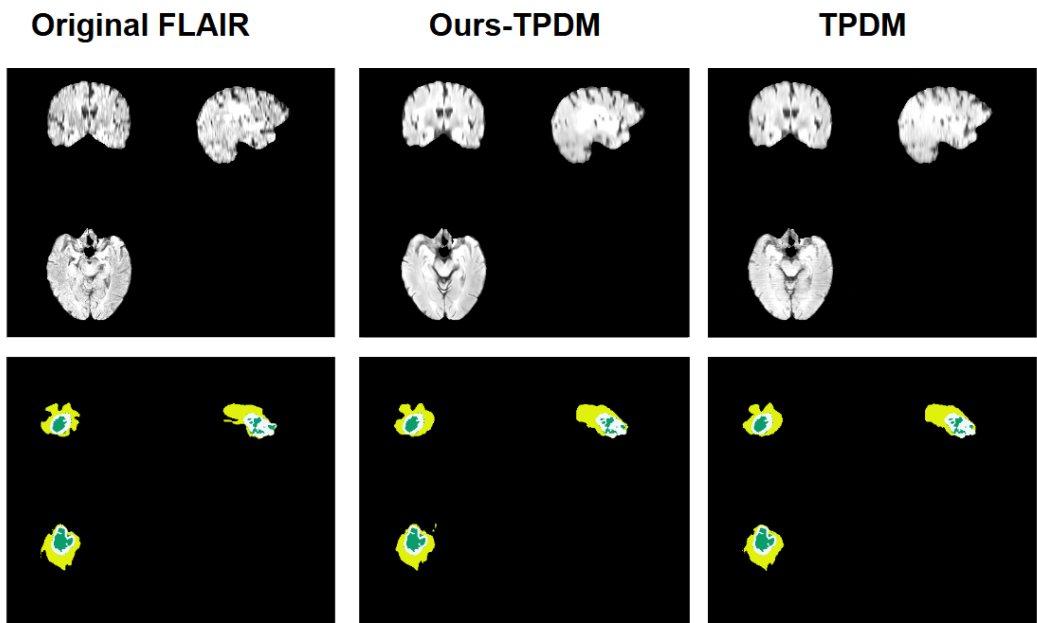


Figure 10. Qualitative results for the downstream task, tumor segmentation, in modality translation task

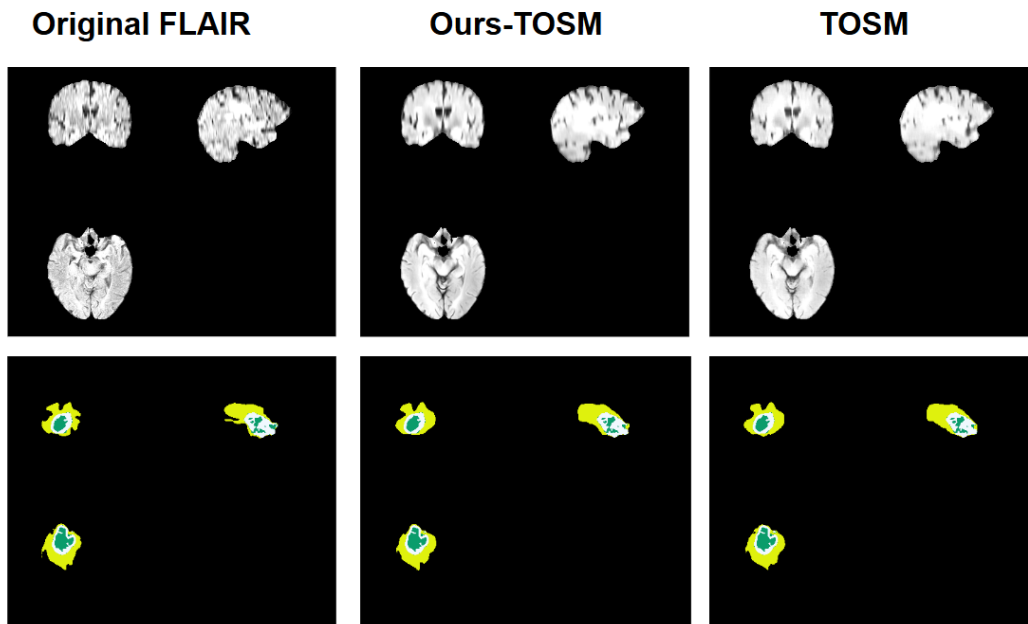


Figure 11. Qualitative results for the downstream task, tumor segmentation, in modality translation task

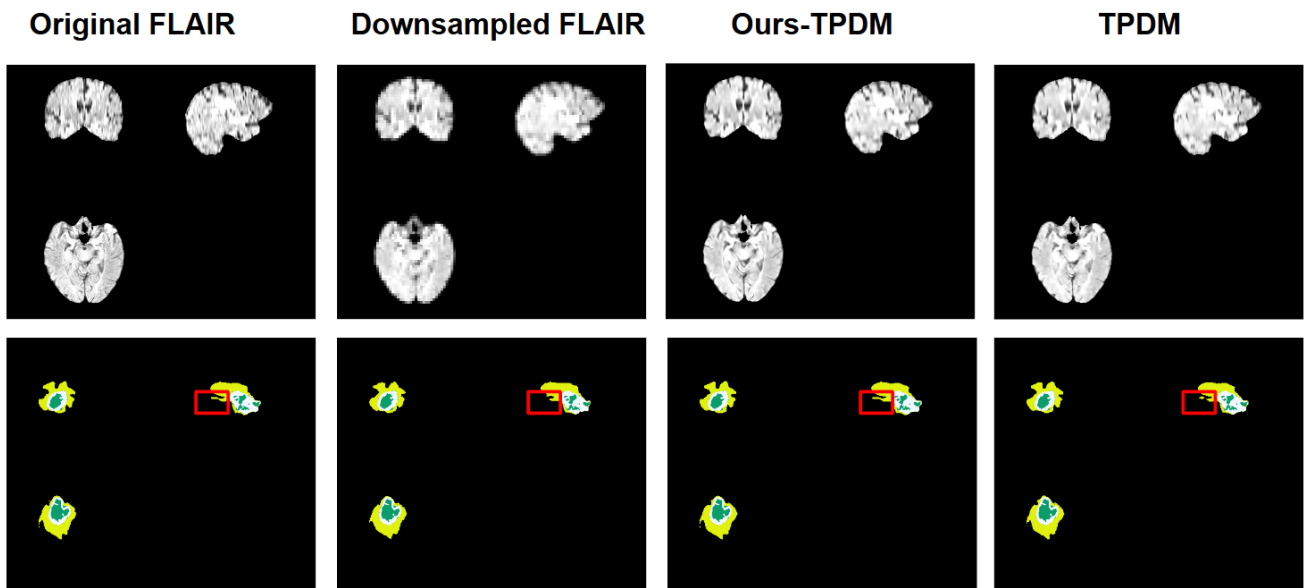


Figure 12. Qualitative results for the downstream task, tumor segmentation, in super-resolution task

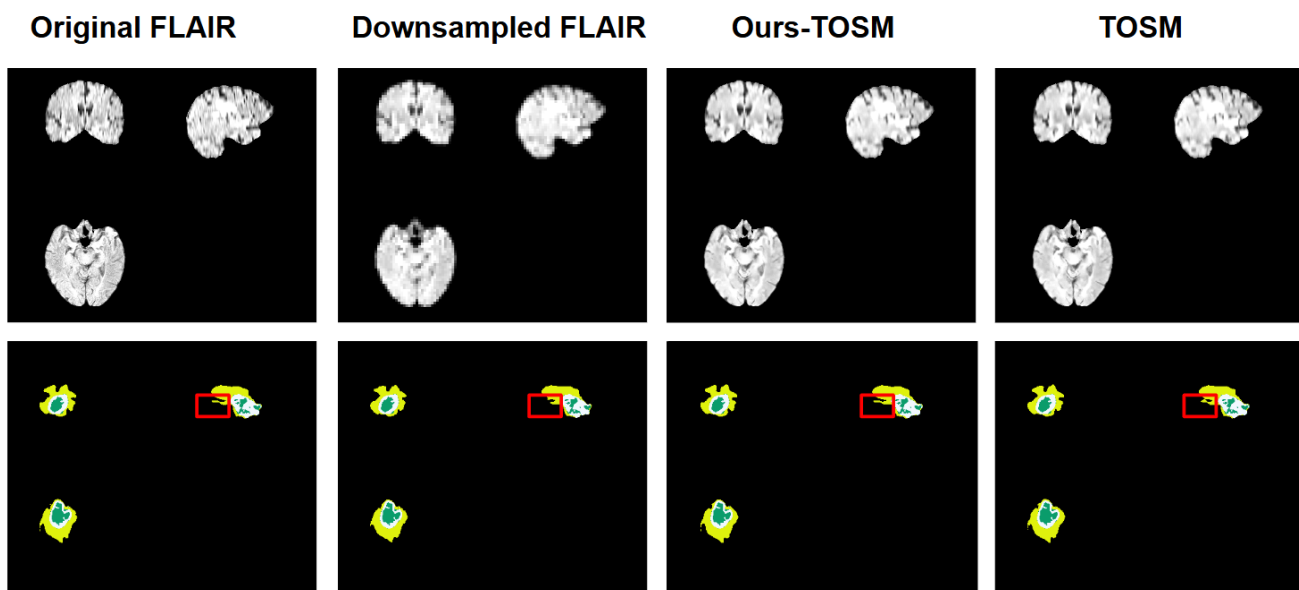


Figure 13. Qualitative results for the downstream task, tumor segmentation, in super-resolution task

Table 9. Architecture for 2D diffusion model. Each ResnetBlock consists of 3 conv2D layers of the same channel and a skip connection. All ResnetBlocks are used with time embedding.

layers		parameters
input	Conv3d	in_ch: 5, out_ch: 64, kernel: 3x3, stride: 1, pad: 1
Time_Embed	Linear Activateion Linear	in_ch:64, out_ch: 256 Swish in_ch:256, out_ch: 256
Downsample_block_1	ResnetBlock ResnetBlock Downsample(Conv3d)	in_ch:64, out_ch: 64 in_ch:64, out_ch: 64 in_ch:64, out_ch: 64,kernel:3x3, stride:2)
Downsample_block_2	ResnetBlock ResnetBlock Downsample(Conv3d)	in_ch:64, out_ch: 128 in_ch:128, out_ch: 128 in_ch:128, out_ch: 128,kernel:3x3, stride:2
Downsample_block_3	ResnetBlock ResnetBlock Downsample(Conv3d)	in_ch:128, out_ch: 256 in_ch:256, out_ch: 256 in_ch:256, out_ch: 256,kernel:3x3, stride:2
Downsample_block_4	ResnetBlock ResnetBlock	in_ch:256, out_ch: 512 in_ch:512, out_ch: 512
Middle	ResnetBlock ResnetBlock	in_ch:512, out_ch: 512 in_ch:512, out_ch: 512
Upsample_block_1	ResnetBlock ResnetBlock Upsample	in_ch:512, out_ch: 512 in_ch:512, out_ch: 512 Conv3d and F.interpolate
Upsample_block_2	ResnetBlock ResnetBlock Upsample	in_ch:512, out_ch: 256 in_ch:256, out_ch: 256 Conv3d and F.interpolate
Upsample_block_3	ResnetBlock ResnetBlock Upsample	in_ch:256, out_ch: 128 in_ch:128, out_ch: 128 Conv3d and F.interpolate
Upsample_block_4	ResnetBlock ResnetBlock	in_ch:128, out_ch: 64 in_ch:64, out_ch: 64
Out	Normalize Activation Conv3d	64 nn.SiLU in_ch:64, out_ch: 1, kernel: 3x3, stride: 1, pad: 1

Table 10. Architecture for 3D diffusion model. Each ResnetBlock consists of 2 conv3D layers of the same channel and a skip connection. All ResnetBlocks are used with time embed with an embedding layer, as well as gradient checkpoint

layers		parameters
input	Conv3d	in_ch: 5, out_ch: 64, kernel: 3x3, stride: 1, pad: 1
Time_Embed	Linear	in_ch:64, out_ch: 256
	Activateion	nn.SiLU
	Linear	in_ch:256, out_ch: 256
Downsample_block_1	ResnetBlock	in_ch:64, out_ch: 64
	ResnetBlock	in_ch:64, out_ch: 64
	Feature_injetced_from_2D	in_ch:64, out_ch: 64)
	Downsample(Conv3d)	in_ch:64, out_ch: 64, kernel:3x3, stride:2)
Downsample_block_2	ResnetBlock	in_ch:64, out_ch: 128
	ResnetBlock	in_ch:128, out_ch: 128
	Feature_injetced_from_2D	in_ch:128, out_ch: 128)
	Downsample(Conv3d)	in_ch:128, out_ch: 128, kernel:3x3, stride:2
Downsample_block_3	ResnetBlock	in_ch:128, out_ch: 192
	ResnetBlock	in_ch:192, out_ch: 192
	Feature_injetced_from_2D	in_ch:192, out_ch: 192)
	Downsample(Conv3d)	in_ch:192, out_ch: 192, kernel:3x3, stride:2
Downsample_block_4	ResnetBlock	in_ch:192, out_ch: 256
	ResnetBlock	in_ch:256, out_ch: 256
	Feature_injetced_from_2D	in_ch:256, out_ch: 256)
Middle	ResnetBlock	in_ch:256, out_ch: 256
	ResnetBlock	in_ch:256, out_ch: 256
Upsample_block_1	ResnetBlock	in_ch:256, out_ch: 256
	ResnetBlock	in_ch:256, out_ch: 256
	Upsample	Conv3d and F.interpolate
Upsample_block_2	ResnetBlock	in_ch:256, out_ch: 192
	ResnetBlock	in_ch:192, out_ch: 192
	Upsample	Conv3d and F.interpolate
Upsample_block_3	ResnetBlock	in_ch:192, out_ch: 128
	ResnetBlock	in_ch:128, out_ch: 128
	Upsample	Conv3d and F.interpolate
Upsample_block_4	ResnetBlock	in_ch:128, out_ch: 64
	ResnetBlock	in_ch:64, out_ch: 64
Out	Normalize	64
	Activation	nn.SiLU
	Conv3d	in_ch:64, out_ch: 2, kernel: 3x3, stride: 1, pad: 1

Table 11. Architecture for the smaller variant of 3D diffusion model. Again, each ResnetBlock consists of 2 conv3D layers of the same channel and a skip connection. All ResnetBlocks are used with time embedding with an embedding layer, as well as a gradient checkpoint. We used a smaller number of channels for each layer and omitted the feature injection from 2D

layers		parameters
input	Conv3d	in_ch: 5, out_ch: 32, kernel: 3x3, stride: 1, pad: 1
Time_Embed	Linear Activateion Linear	in_ch:32, out_ch: 128 nn.SiLU in_ch:128, out_ch: 128
Downsample_block_1	ResnetBlock ResnetBlock Downsample(Conv3d)	in_ch:32, out_ch: 32 in_ch:32, out_ch: 32 in_ch:32, out_ch: 32,kernel:3x3, stride:2)
Downsample_block_2	ResnetBlock ResnetBlock Downsample(Conv3d)	in_ch:32, out_ch: 64 in_ch:64, out_ch: 64 in_ch:64, out_ch: 64,kernel:3x3, stride:2
Downsample_block_3	ResnetBlock ResnetBlock Downsample(Conv3d)	in_ch:64, out_ch: 64 in_ch:64, out_ch: 64 in_ch:64, out_ch: 64,kernel:3x3, stride:2
Downsample_block_4	ResnetBlock ResnetBlock	in_ch:63, out_ch: 128 in_ch:128, out_ch: 128
Middle	ResnetBlock ResnetBlock	in_ch:128, out_ch: 128 in_ch:128, out_ch: 128
Upsample_block_1	ResnetBlock ResnetBlock Upsample	in_ch:128, out_ch: 128 in_ch:128, out_ch: 128 Conv3d and F.interpolate
Upsample_block_2	ResnetBlock ResnetBlock Upsample	in_ch:128, out_ch: 64 in_ch:64, out_ch: 64 Conv3d and F.interpolate
Upsample_block_3	ResnetBlock ResnetBlock Upsample	in_ch:64, out_ch: 64 in_ch:64, out_ch: 64 Conv3d and F.interpolate
Upsample_block_4	ResnetBlock ResnetBlock	in_ch:64, out_ch: 32 in_ch:32, out_ch: 32
Out	Normalize Activation Conv3d	64 nn.SiLU in_ch:32, out_ch: 2, kernel: 3x3, stride: 1, pad: 1

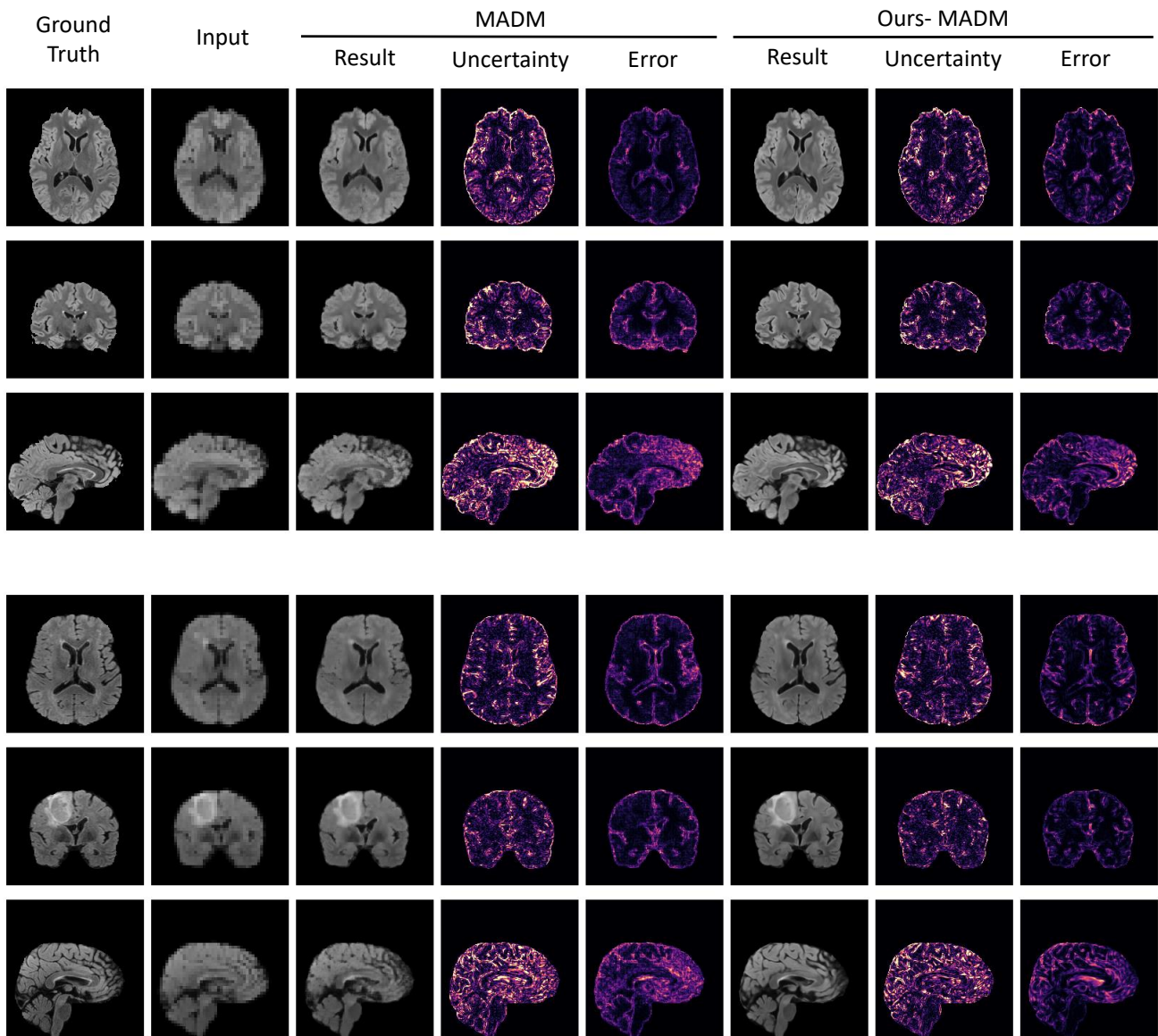


Figure 14. Uncertainty awareness results on super-resolution task

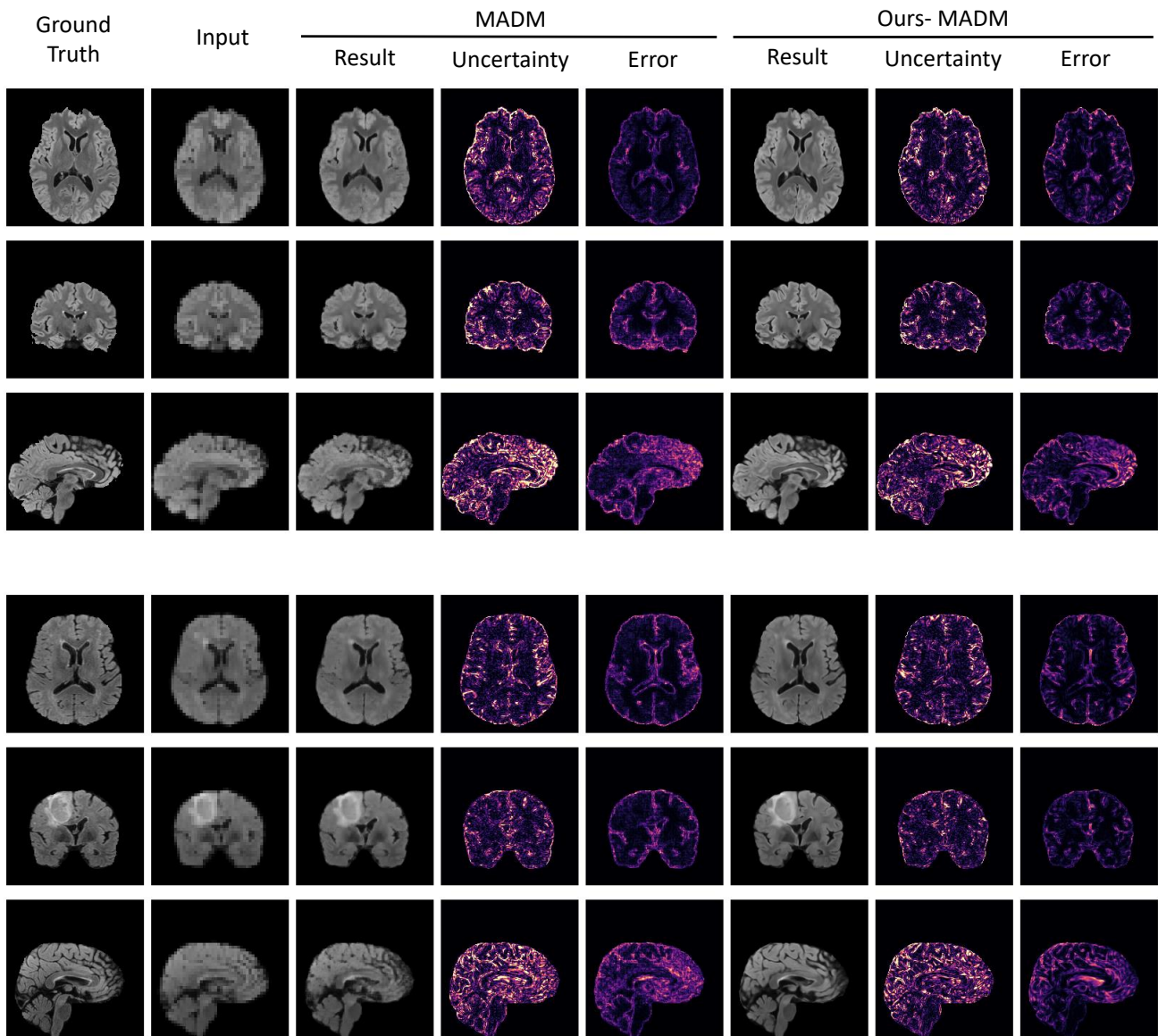


Figure 15. Uncertainty awareness results on super-resolution task

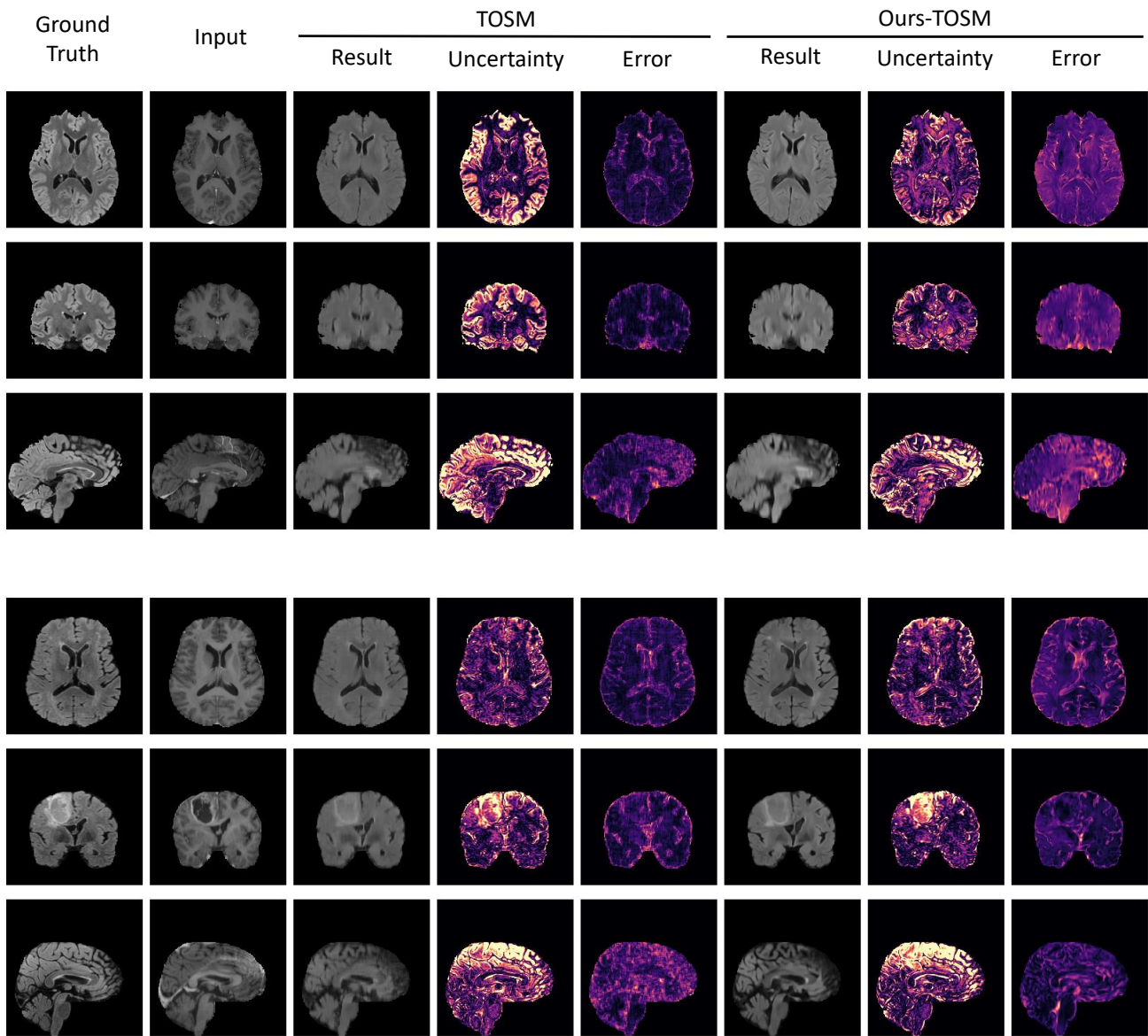


Figure 16. Uncertainty awareness results on modality translation task

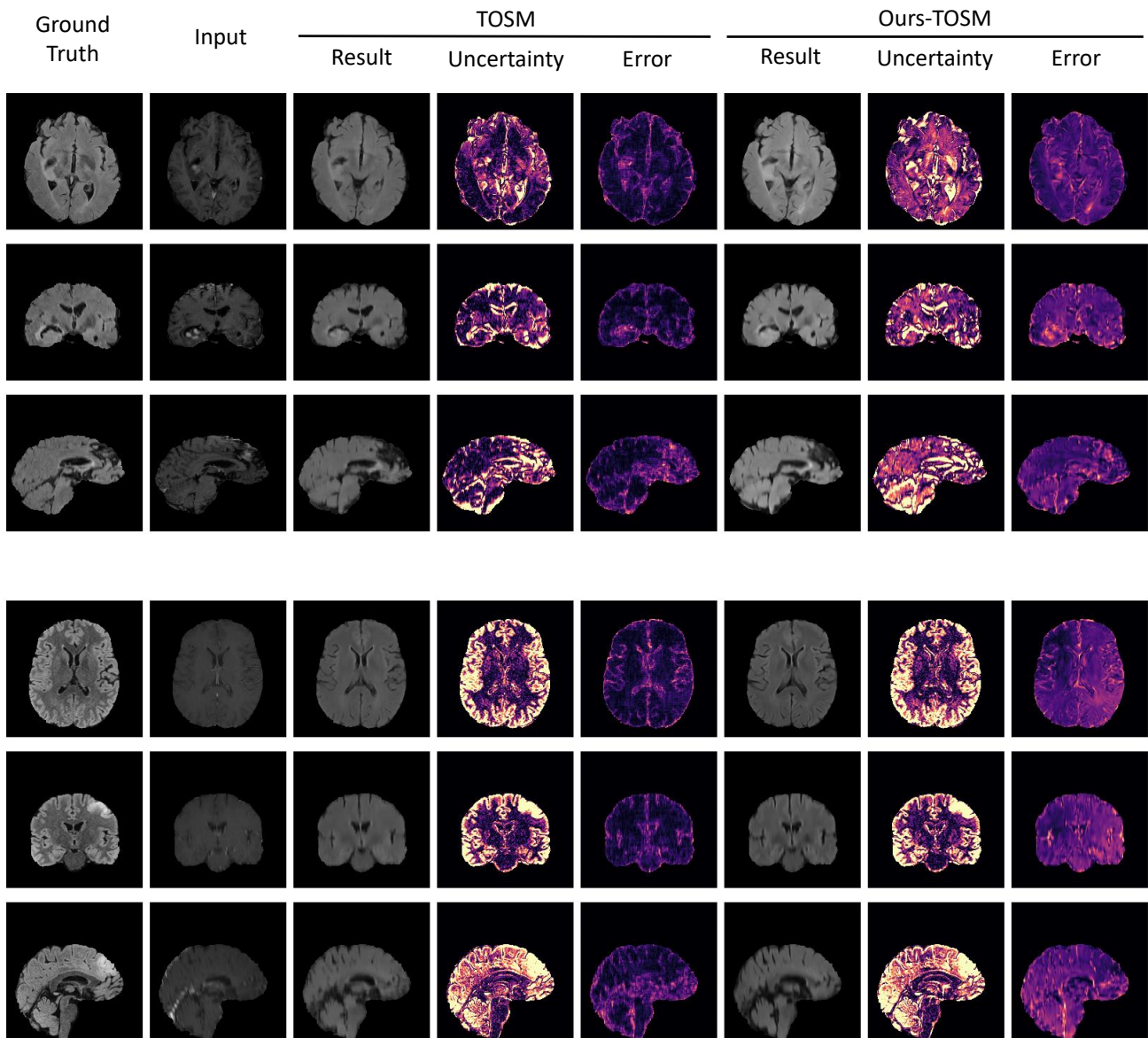


Figure 17. Uncertainty awareness results on modality translation task

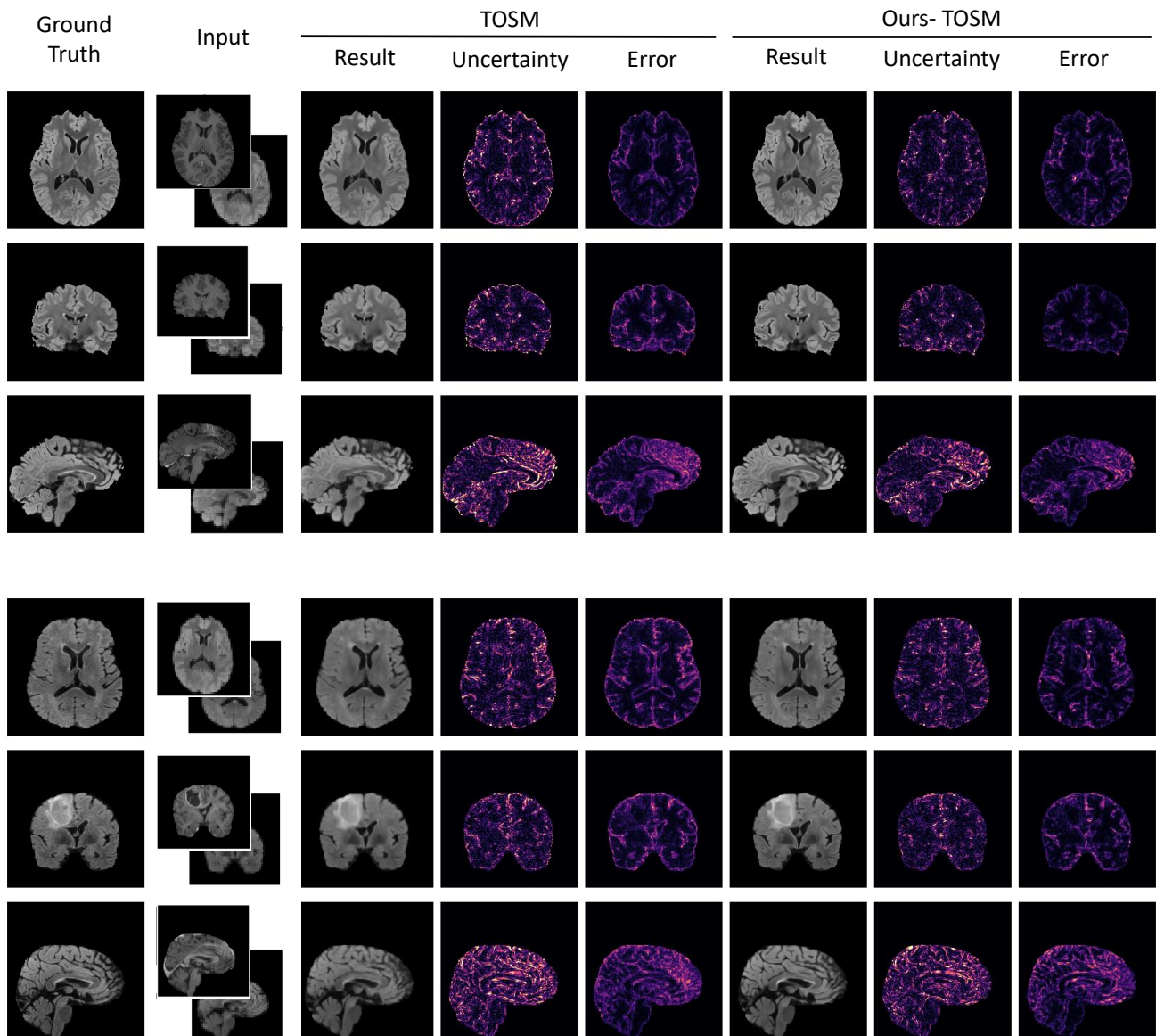


Figure 18. Uncertainty awareness results given both conditions

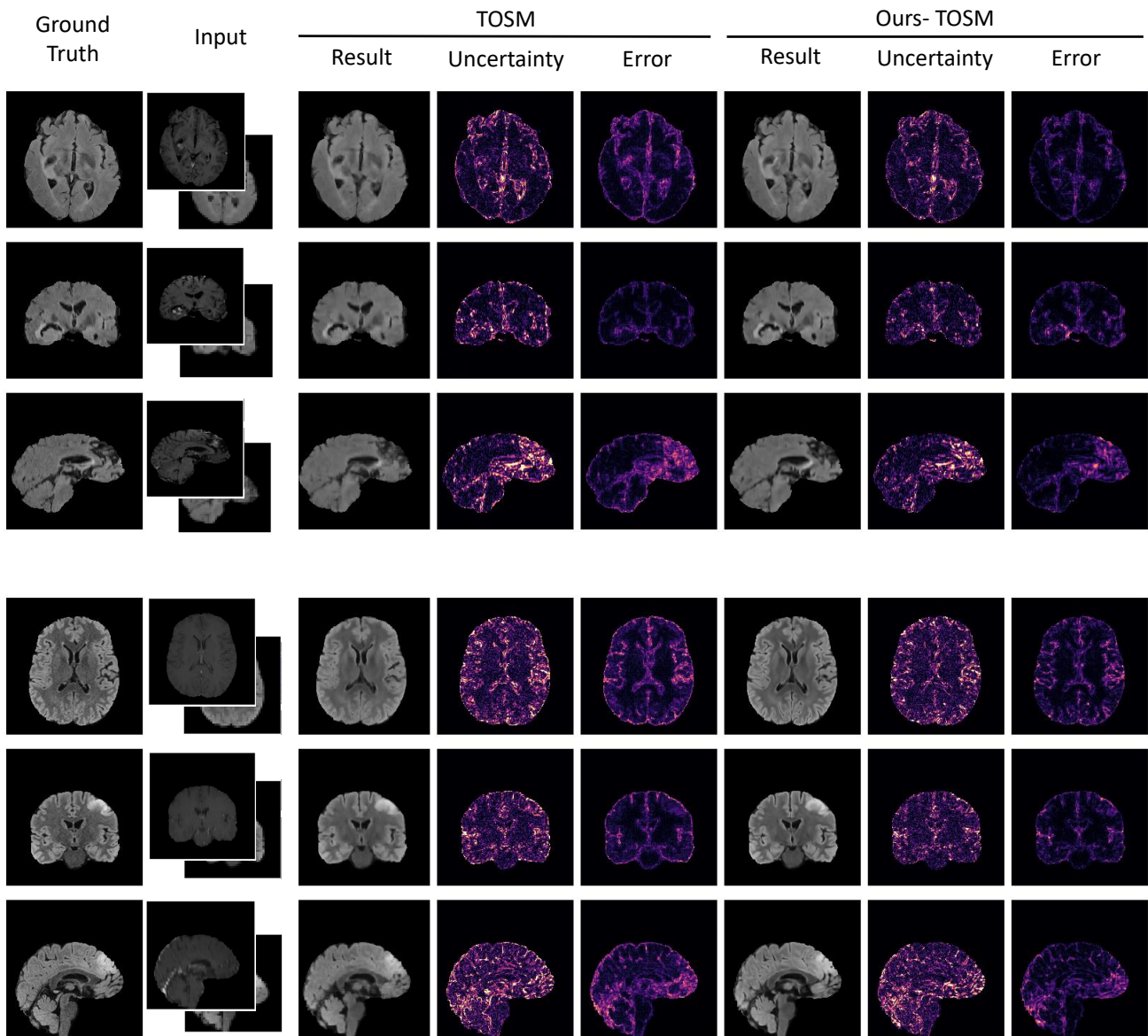


Figure 19. Uncertainty awareness results given both conditions

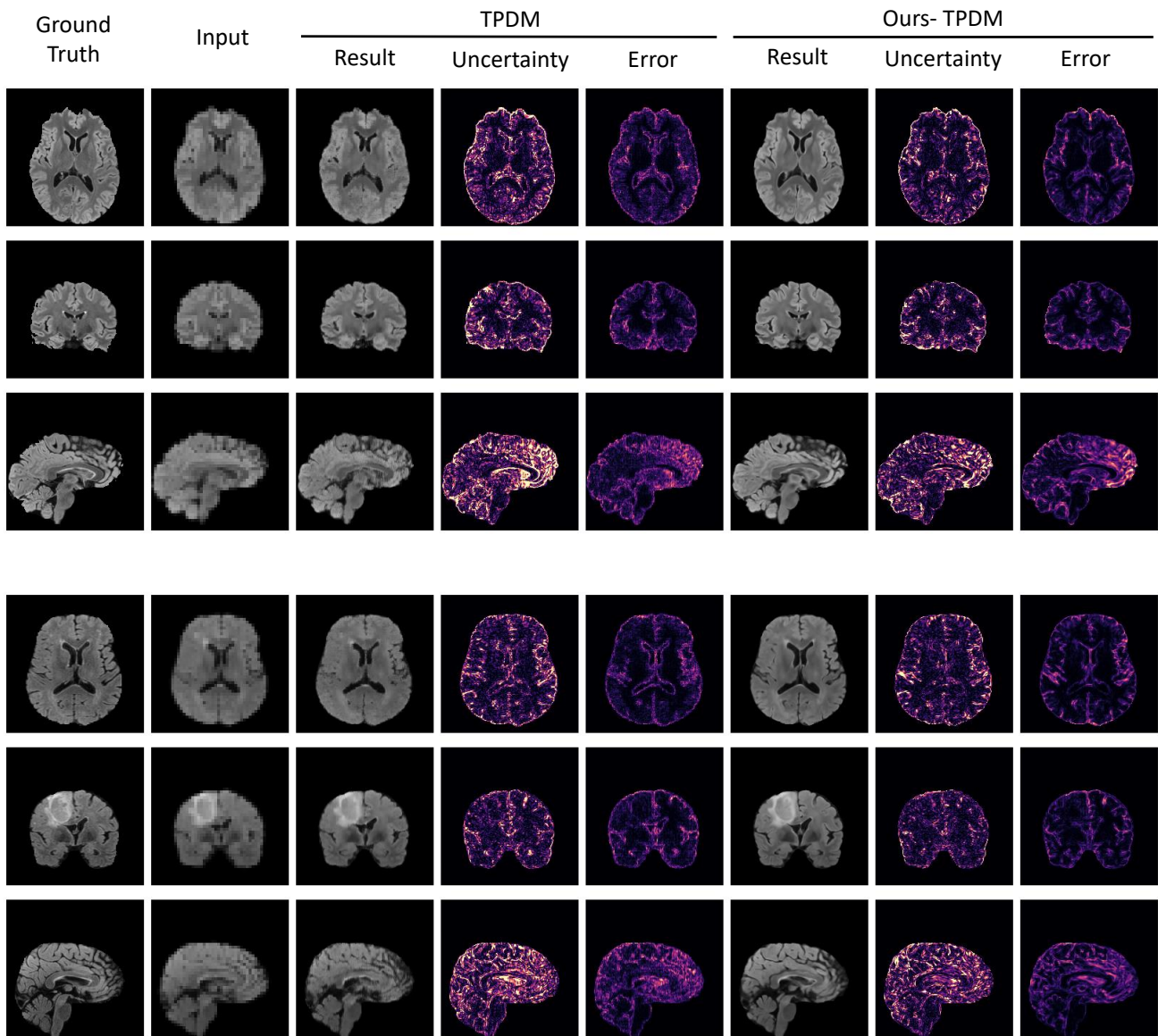


Figure 20. Uncertainty awareness results on super-resolution for TPDM and Ours-TPDM

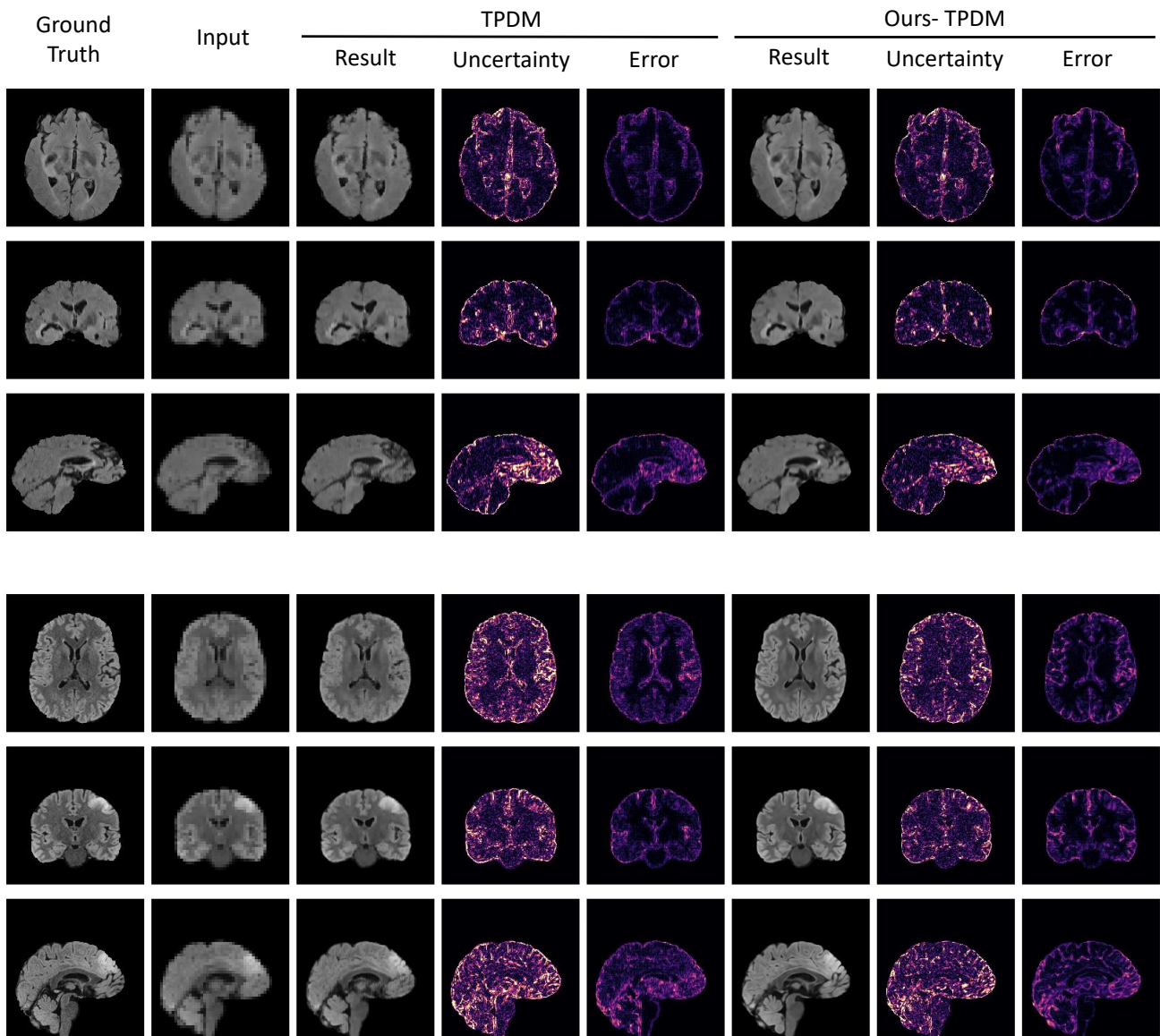


Figure 21. Uncertainty awareness results on super-resolution for TPDM and Ours-TPDM